DOPANT ACTIVATION IN SUB-MILLISECOND LASER SPIKE ANNEALED $IN_{0.53}GA_{0.47}AS$

A Thesis

Presented to the Faculty of the Graduate School

of Cornell University

In Partial Fulfillment of the Requirements for the Degree of

Master of Science

by

Suki Naifang Zhang

August 2015

ABSTRACT

InGaAs has garnered considerable attention as a potential alternative to silicon for continuing progress along Moore's Law. While it has good electrical properties, it is difficult to activate silicon dopants in InGaAs. Using Laser Spike Annealing (LSA), we show that dopant activation can be improved the thermal budget of InGaAs and extended. The absolute temperature under LSA was determined using thin film Pt thermistors calibrated using a known polymer's decomposition temperature. Raman spectroscopy was used to spatially probe the InGaAs film quality and dopant activation level after furnace and LSA. CAPRES 4-point measurements confirm that values of the sheet resistance as a function of annealing temperature match well with results from the Raman analysis. We show that LSA is effective in increasing carrier activating for samples pre-anneal using rapid thermal processing techniques. Overall, this work demonstrates that LSA is effective in enhancing the electrical behavior of InGaAs.

BIOGRAPHICAL SKETCH

Suki was born on May 26th, 1990 in Shenzhen, China and moved to the United States in her high school sophomore year.

She enters college in 2008 and her interests in materials science ignited during her freshman summer experience in the Princeton University REU program. Her project was to characterize the optical properties of Lithium Niobate, an optical waveguide material. After the summer, she participated in Professor Qibing Pei's soft material lab for almost three years at University of California, Los Angeles (UCLA). In the mean time, Suki worked on several projects including fabrication and examination of polymeric composite actuators and different nanoparticles synthesis.

After obtaining her Bachelor of Science degree in Materials Engineering from UCLA in March 2013, she continued her master study at Cornell University in August 2013. She was fortunate working with Professor Michael Thompson in the thermal transient lab and her master thesis focused on using sub-millisecond laser spike annealing to improve InGaAs electrical performance for future channel material purpose. She received the Master of Science degree in Materials Science Engineering in May 2015 from Cornell University.

Suki was inspired and motivated to pursue a Ph.D degree. She will attend Purdue University in the Electrical Computer Engineering department upon graduation and conduct research on 2D field effect transistor devices.

Dedicated to God and My Family

ACKNOWLEDGMENTS

I would like to express my sincere gratitude and respect to my advisor Professor Michael Thompson for his advice and support of my research. His critique of the experimental data as well as this manuscript is greatly appreciated. I want to thank him for always being patient to me and help me out when I face obstacles.

I am particularly grateful to Professor Paulette Clancy to be my committee and all the supports and suggestions she provided me during our subgroup meetings. I was highly encouraged and gained confidence every time we had eye contact during my past presentations.

I am also thankful to obtain the opportunity, provided by Professor Thompson and Professor Clancy, to present my research at the SRC TechCon 2014, which broadening up my vision towards my future research.

It is my pleasure to give special thanks to my subgroup members Megan Hill, Xuetian Ma, Chinmaya Joshi in Thompson's group and Victoria Sorg, Jingyang Wang, Mardochee Reveil, Dr. Binit Lukose, Cheng-wei Lee in Clancy's group. We had numerous hours of inspiring, fruitful, enjoyable discussions and I learned so much from them in all aspects.

I also want to thank my other colleagues in Thompson's group, Dr. Bin Zhu, David Lynch, Chen-yang Chung, Wenjin Zhang, Zeming Sun, Alan Jacobs, Robert Bell and Jing Jiang. It is my pleasure to work with these smart and friendly people. Their helps have been greatly appreciated.

I would like to thank SRC for the funding and IBM for providing samples to this project. I also like to give thanks to Professor Kevin Jones at University of Florida for the collaborations. All Cornell Nanofabrication Facilities (CNF) and Cornell Center of Materials Research (CCMR) staff and members are gratefully acknowledged.

I am fortunate to meet my roommate Chang Lau again at Cornell University, who has been my best friend since middle school. I want to thank her for being such a good friend for more than half of my lifetime so far. I also want to thank my friend Raymond Co who is currently working on his Ph.D degree in Physics at University of California, Berkeley. He has been such a worthwhile friend who helps me to find resources and advices me towards my academic dreams. There are so many people I want to give thanks, but not able to list all of them. I am glad to have many good friends from high school, college, graduate school and church. Their supports and love are always incredibly meaningful to me.

Mostly, I must sincerely thank my parents for their unfailing love, numerous sacrifices, their confidence and moral support throughout my educational endeavors. Without them for always being there for me wherever I go, there would not be me like this and my thesis written.

TABLE OF CONTENTS

LIST OF FIGURES

Figure 2.7: CO_2 beam profile in the x- and y- directions. The FWHMs of the x-direction is 90.3 μm and the y-direction is 588.2 μm. Both directions are Gaussian in shape. The center (red) is in hotter than outside (green and light blue).

Figure 2.8: Diode beam profile in the x- and y- directions. The FWHMs of the x-direction is 1564.3 μm and the y-direction is 301.7 μm. The x- direction is in trapezoidal shape and the y-direction is roughly Gaussian.

Figure 2.9: Thermistor device layout is shown on the left. The six gray squares are the contact pads. The lines in the middle are Pt thermal resistor wires. The image on the right shows the detail of the thermistor itself. The specific dimensions are labeled on the right graph.

Figure 2.10: Optical image of the fabricated thermistor. The scale bar is 10 μm.

Figure 2.11: Schematic cross-section of the thermistor: 40 nm Pt resistor with 2 nm Cr adhesion layer, 40 nm insulation layer and 250 nm of Ni for the contact pads.

Figure 2.12: Spatial profile for a 500 μs dwell at different values of the laser power under CO_2 LSA. The increasing power provides higher temperature to the sample, resulting in higher resistance changes to the Pt thermistor. The peak temperature for 16 W is approximately twice that of the 8 W conditions.

Figure 2.13: Schematic of polymer decomposition calibration after LSA. For the photoresist layer, the annealing temperature increases from left to right. The polymer first is activated by laser power and slowing decomposes with increasing annealing temperature.

Figure 2.14: Optical image of an S1815 polymer film after LSA. From the left to right, the photoresist get annealed at higher laser powers. As a consequence, the centers of the annealing region (white) get wider with the increasing laser temperature.

Figure 2.15: Profilometer measurement of polymer decomposition at 250 μs for S1805 decomposition on Si. Red curve shows partial decomposition at 1000 ^{o}C. Green curve shows onset of full decomposition with center reaching 1100 ^{o}C. Blue curve shows full decomposition with the center reaching 1200 ^{o}C.

Figure 2.16: Calibration curves for thermistor measurements under LSA using CO_2 laser at different dwells. The specific power is plotted in x axis for each dwell with corresponding annealing temperatures on the left axis and resistances on the right axis.

Figure 2.17: Temperature spatial profile at 1 ms dwell and 24W annealing power under CO_2 LSA. The peak temperature at center is ~850 ^{o}C and cooler away from either side.

Chapter 3

Chapter 4

APPENDIX

LIST OF TABLES

CHAPTER 1

INTRODUCTION

1.1 Motivation

Si transistors have been the main building blocks of modern electronic devices technology since 1965 [1]. With Moore's Law suggesting that the number of transistors on a microchip should double every 18 months, primarily through the size reduction of transistor components. However, silicon is reaching the material's intrinsic limits and will be difficult to scale below the 10 nm node [2]. New materials are still required to fabricate smaller, faster, and higher energy efficiency devices, allowing Moore's Law to continue to hold for further generation.

Among all the potential options for scaling, such as 3D tri-gates transistor, reduced gate length and high-k dielectric gate oxides, InGaAs has emerged as a strong alternative to silicon n-channel devices. InGaAs is an attractive candidate due to its high intrinsic mobility, moderate bandgap, and low interface density of states. Figure 1.1 shows a novel n-type InGaAs quantum-well (QW) metal–oxide–semiconductor field-effect transistor (MOSFET) recently fabricated by researchers at MIT [3].

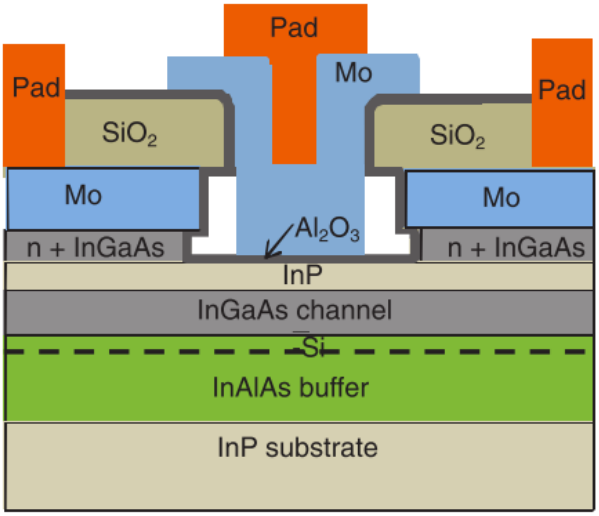

Figure 1.1: The cross-sectional schematic of an n-type InGaAs quantum-well (QW) metal–oxide–semiconductor field-effect transistor (MOSFET) fabricated by MIT [3]

The conductivity (σ) and the performance of the channel material can be improved using a high mobility material ($\mu_e \; or \; \mu_p$) and obtaining a high carrier concentration ($n \; or \; p$):

$$\sigma = ne\mu_e + pe\mu_p \qquad (1.1)$$

The electron mobility of InGaAs is high enabling faster switching devices. Using transient thermal annealing (laser spike annealing), we believe that higher carrier concentrations can be obtained while maintaining the high mobility. In this thesis, we explore this hypothesis using laser spike annealing, extending the thermal budget before damage and improving the dopant activation of InGaAs.

1.2 InGaAs

Indium gallium arsenide is a ternary III-V alloy of indium, gallium and arsenic. Indium and gallium atoms sit on the group III cation sites and the arsenic atoms sit on group V anion sites.

InGaAs has excellent electronic properties, such as an electron mobility of 10,000 cm^2/V-s, which is 6 times higher than that of silicon. Even at high dopant concentrations, the mobility of InGaAs still exceeds 1500 cm^2/V-s [4]. The high electron mobility and low current leakage properties of InGaAs come from the high electron mobility of InAs and the large bandgap of GaAs. Much of the focus on this material has been on a specific composition of InGaAs, namely $In_{0.53}Ga_{0.47}As$, because it is a lattice-match with that of InP substrates, so that no strain created in samples that contain them.

Using InGaAs as a replacement channel material in high performance circuits, electronic devices can have a lofi3wer power dissipation while maintaining a high speed as compared with traditional silicon channels. InGaAs is also compatible with existing fabrication processes, as compared to other high mobility materials such as carbon nanotubes or 2D nanowires. Overall, InGaAs appears to be a promising material for future devices.

Although InGaAs is a favorable material performance, it is not yet been used commercially in highly integrated circuits. There are still many challenges that need to be solved before its practical usage, including the fact that InGaAs is not compatible with a silicon substrate and is known to have a poor channel/oxide interfacial quality. The thermal limits of InGaAs are known to be low before material damage during

traditional annealing. Arsenic has a low vapor pressure and it evaporates at a much lower temperatures as compared to In and Ga. In order to prevent As evaporation, many groups coat a layer of aluminum oxide to protect the InGaAs surface [5], this oxide cap prevents As atom from escaping from the InGaAs lattice at normal annealing temperatures [6].

Silicon, which is a common dopant for InGaAs, behaves in an amphoteric way. Silicon can substitute on either cation sites or anion sites in the InGaAs lattice; on cation site, so acts as a donor while on anion sites it acts as an acceptor. When substituting on both cation and anion sites, this results in a self–compensation of dopants, which then limits the total activation. Since Si-doped InGaAs is intended for use in n-channel devices, silicon preferably showed sit only on cation sites. A schematic lattice of Si-implanted InGaAs is shown in Figure 1.2.

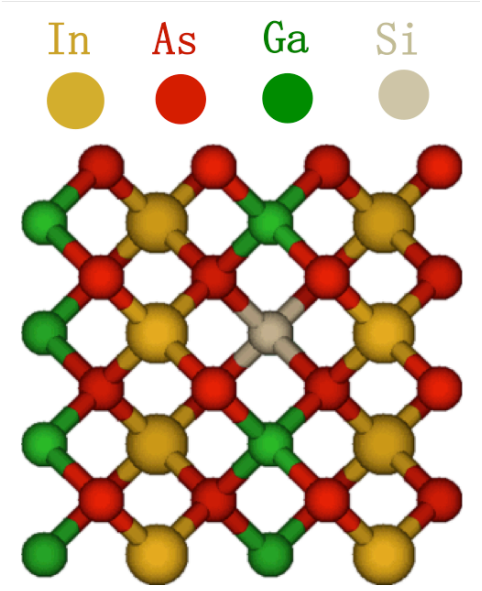

Figure 1.2: A schematic for Si atom (gray) sitting on a cation site (yellow or green) in a Si^{+}-implanted InGaAs lattice [7].

At a high implant concentrations, silicon is also known to be troublesome in terms of forming silicon clusters as opposed to isolated sites, this also limits the effectiveness of dopant activation [8]. From literature, InGaAs appears to have an equilibrium solubility of Si of 1.5 x 10^{19} cm^{-3}, as shown in Figure 1.3 [5]. The goals of this project are not only to obtain higher dopant solubility in the InGaAs matrix, but also to achieve higher dopant activation.

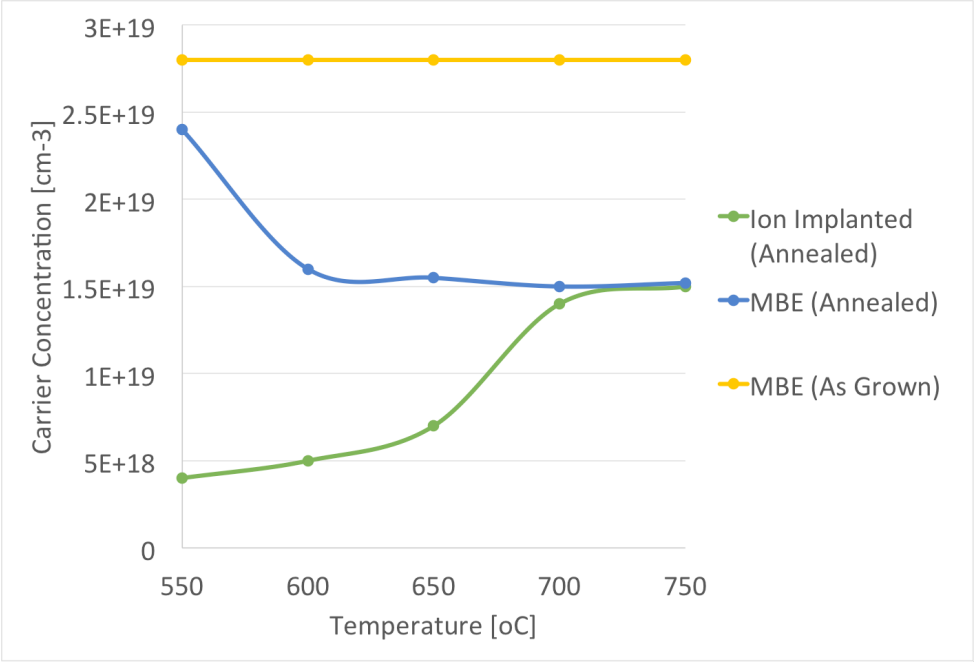

Figure 1.3: The InGaAs dopant solubility limit established by Jone's group at the University of Florida. The ion-implanted Si concentration in InGaAs increases with higher annealing temperature and reaches the threshold limits at 1.5 x 10^{19} cm^{-3} via furnace annealing. For MBE grown Si doped InGaAs samples, Si is deactivated to the same limiting concentration further annealing [5].

1.3 Laser Spike Annealing

Traditional annealing methods, such as furnace annealing and rapid thermal annealing (RTA), use thermal energy to activate the dopants in InGaAs on seconds to hours timescales [9]. In contrast, laser spike annealing (LSA) reaches much higher temperatures for shorter times, as shown schematically in Figure 1.4. With rapid heating and quenching rates of 10^4-10^5 K/s using LSA, sufficient thermal energy can be provided to allow intrinsic defects to be removed, and to dissolve any existing dopant defect clusters. Since LSA also operates on a short timescale compared with traditional annealing methods, there is limited dopant diffusion. Laser spike annealing potentially enables dopants sitting at desired metastable states to reach favored substitutional sites while preventing long range diffusion.

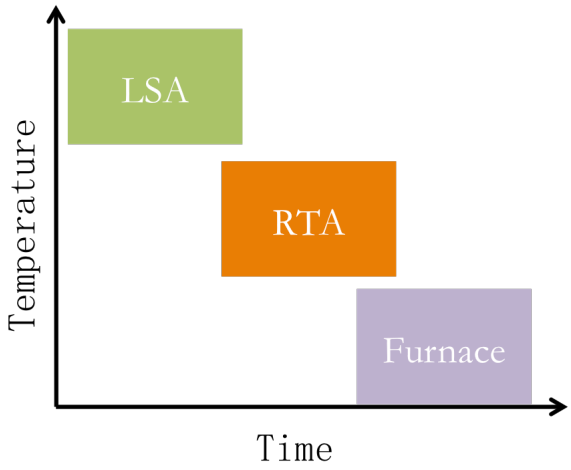

Figure 1.4: The differences among different annealing methods in terms of temperature and time scales.

Laser spike annealing can also provide a better option for selectively annealing certain regions in the device. Furnace annealing and rapid thermal annealing generally

affect a large area uniformly and it is difficult to anneal limited parts of the structure. Using laser spike annealing, specific location or structure in the sample can be annealed without impacting the neighboring environment.

Samples were laser spike annealed at different conditions using single laser scan across each sample at a sub-millisecond time scale. Figure 1.5 shows a schematic of laser spike annealing the sample due to the Gaussian shape of the laser beam; the center of the annealing region reaches a higher temperature than those further from the center. This has the advantages that many annealing conditions on the sample are accessed at once across the annealing region with one single scan.

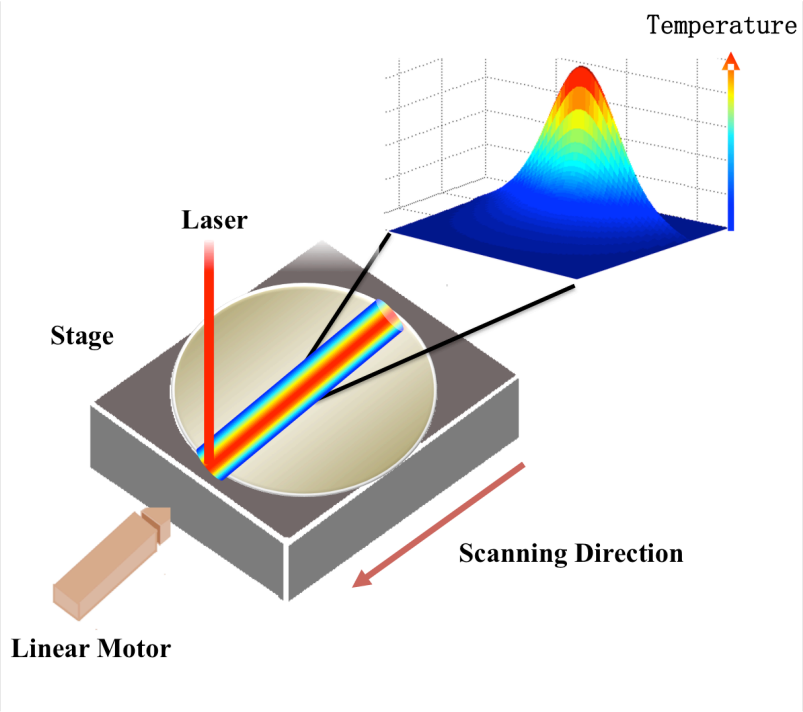

Figure 1.5: A schematic for laser spike annealing performed on the InGaAs sample; the laser beam (red) in focused to a line through cylindrical lens and scan across the sample in the direction indicated by the arrow. The annealing profile is hottest at the center and cooler to either side.

There are two key variables that control the annealing conditions, laser power and dwell time. In order to fully understand the temperatures accessed under laser spike annealing, it is important to determine the absolute temperatures. Previous work in our group developed a technique to calibrate absolute temperatures on silicon during laser spike annealing using specially fabricated platinum thermistors [10]. Using this technique, the change in resistivity of the thermistors is directly proportional to the temperature and can be measured as a function of time and position relative to the laser center. For InGaAs, we used a polymer with a known decomposition temperature to obtain absolute temperatures. Additional details on laser spike annealing and the InGaAs temperature calibrations are discussed in Chapter 2.

1.4 Raman Characterizations

The Indian Scientist C.V. Raman who earned the Nobel Prize for Physics on 1930, is credited with discovering Raman scattering. He noted that scattered light would change in wavelength when the incident light transverses through a transparent material; this is known as the Raman effect.

In this work, Raman spectroscopy has been used extensively to characterize I Si^+ implanted InGaAs at different annealing temperatures under laser spike annealing conditions. Raman is a non-destructive optical technique to assess film quality, composition and stress in thin films. Thermal limits to InGaAs under laser spike annealing can be established using our knowledge of the InGaAs thermistors and analysis of the Raman peaks. A number of InGaAs samples were characterized with different conditions: low dose implants samples, high dose implants samples, samples

with Al_2O_3 capping layer, capless samples and the MBE grown samples. In order to compare laser spike annealing with traditional annealing methods, we also studied the effect of the furnace annealing on InGaAs samples. Chapter 3 primarily discusses the Raman analysis of laser spike annealed and furnace annealed InGaAs.

1.5 Electrical Measurements

Electrical measurements of Si^+ implanted InGaAs following laser spike annealing were obtained using the micro Van der Pauw technique known as CAPRES [11]. CAPRES measures the sheet resistance and conductance of Si^+ doped InGaAs at high resolution using ~20 μm scale four-point probes [8]. As we shall see in Chapter 4, CAPRES results were found to match well with the dopant activation extracted using Raman spectroscopy.

REFERENCES

[1] Ferain, Isabelle, Cynthia A. Colinge, and Jean-Pierre Colinge. "Multigate transistors as the future of classical metal-oxide-semiconductor field-effect transistors." *Nature* 479.7373 (2011): 310-316.

[2] Wu, Jerry, Yin-Lin Shen, Kitt Reinhardt, Harold Szu, and Boqun Dong "A nanotechnology enhancement to Moore's law." *Applied Computational Intelligence and Soft Computing* 2013 (2013): 2.

[3] Lin, Jianqiang, Jianqiang Lin, Tae-Woo Kim, Dimitri A. Antoniadis and Jesús A. del Alamo"A self-aligned InGaAs quantum-well metal–oxide–semiconductor field-effect transistor fabricated through a lift-off-free front-end process." *Applied Physics Express* 5.6 (2012): 064002.

[4] Del Alamo, Jesús A. "Nanometre-scale electronics with III-V compound semiconductors." *Nature* 479.7373 (2011): 317-323.

[5] Lind, Aaron G., Henry L. Aldridge Jr., Cory C. Bomberger, Christopher Hatem, Joshua M. O. Zide and Kevin S. Jones. "Comparison of thermal annealing effects on electrical activation of MBE grown and ion implant Si-doped $In_{0.53}Ga_{0.47}As$." *Journal of Vacuum Science & Technology B* 33.2 (2015): 021206.

[6] Jones, Kevin S., Aaron G. Lind, Chris Hatem, Steve Moffatt and Mark C. Ridgeway "(Invited) A Brief Review of Doping Issues in III-V Semiconductors." *ECS Transactions* 53.3 (2013): 97-105.

[7] Jingyang Wang, private communication.

[8] Georgakilas, Alexandros, Athanasios Dimoulasa, Aristotelis Christou and John Stoemenos. "Alloy clustering and defect structure in the molecular beam epitaxy of $In_{0.53}Ga_{0.47}As$ on silicon." *Journal of materials research* 7.08 (1992): 2194-2204.

[9] Penna, Thereza, B. Tell, A. S. H. Liao, T. J. Bridges and G. Burkhardt. "Ion implantation of Si and Se donors in $In_{0.53}Ga_{0.47}As$." *Journal of applied physics* 57.2 (1985): 351-354.

[10] Jung, Byungki. "Laser-Induced Millisecond Heating Of Polymers And Small Molecules For Pattern Development." Ph.D thesis, Cornell University, (2014).

[11] Petersen, Christian L., CAPRES A/S, Burnaby, BC Lin, Rong ; Petersen, D.H. ; Nielsen, P.F.. "Micro-scale sheet resistance measurements on ultra shallow junctions." *Advanced Thermal Processing of Semiconductors, 2006. RTP'06. 14th IEEE International Conference on*. IEEE, 2006.

CHAPTER 2

LASER SPIKE ANNEALING

2.1 LSA Experimental Set-Up

The experimental set-up for the laser spike annealing at Cornell University is shown in Figure 2.1. Two types of laser spike annealing lasers were used in this system: one a CO_2 laser and the other a diode laser. Both the CO_2 laser and the diode laser provide the primary energy source. An attenuator is used to adjust the laser power. There are two shutters to control the laser beam, a safety shutter and a computer controlled process shutter. With both shutters open, the laser beam is allowed to be incident on the x-y stage with the samples. The dwell time varies from ~100 μs to ms time frames depending on the laser source. The dwell time of the laser spike annealing is defined as the full width half maximum (FWHM) of the beam in the direction of motion divided by the stage velocity. In our experiments, there were two major variables, the laser power and the dwell time; these variables allowed different annealing conditions to be experienced by samples.

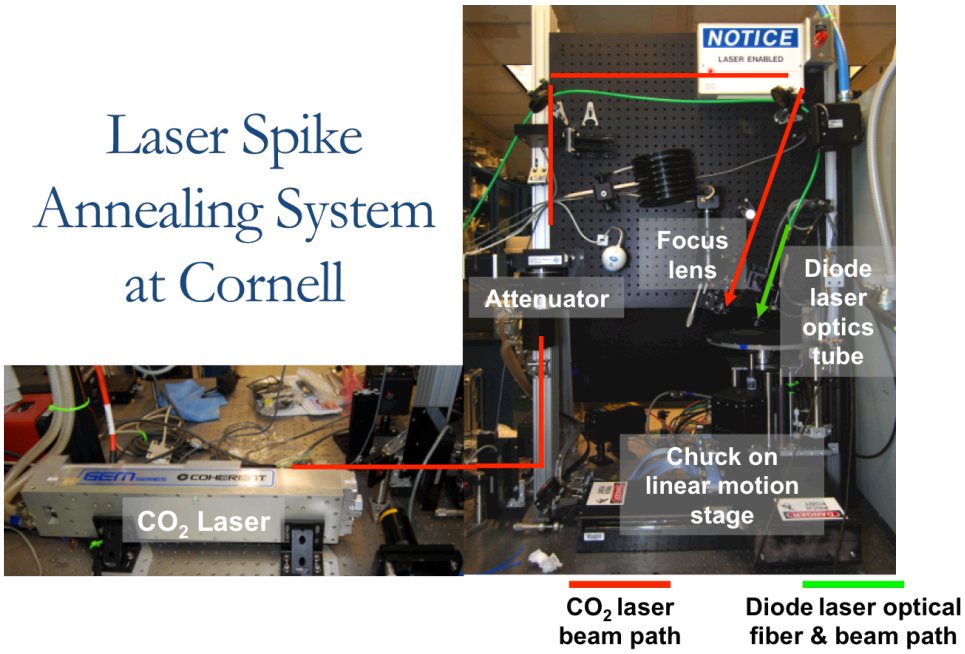

Figure 2.1: Photograph of the experimental LSA systems at Cornell University (Thompson Laboratory). The laser beam passes first through attenuator and focusing lens, before the sample is incident on a moving stage.

2.2 Mechanism of Laser Spike Annealing

Laser spike annealing (LSA) is a powerful technique to activate Si^+ -implanted InGaAs. Utilizing a line-focused laser to scan over the surface of the sample, laser spike annealing can achieve heating rates of 10^6 K/s and quench rates of 10^5 K/s (Figure 2.2). The peak temperature for laser spike annealing is limited only by meting of Si at 1410 °C. The fast scanning rate and high energy provided by the single wavelength laser beam enable metastable silicon dopant activation for both deep-source-drain and shallow implants. Hence laser spike annealing is a promising candidate for thermal processing and has been shown to provide more spatially selective annealing conditions.

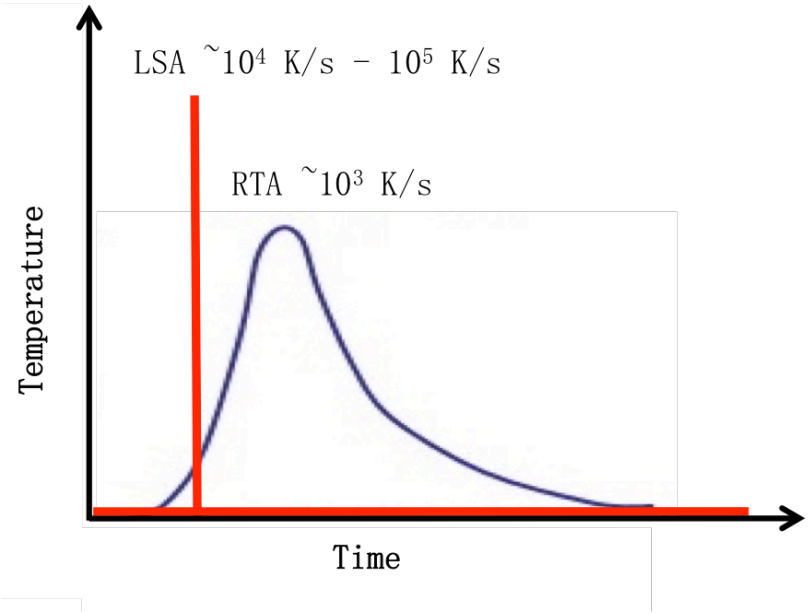

Figure 2.2: Schematic comparison of the temperature-time profiles for heating and quenching obtained by rapid thermal annealing and lasers spike annealing.

2.3 Experiment Overview

InGaAs samples studied were provided either by IBM (through Dr. Phil Oldiges) or from our collaborator Professor Kevin Jones at the University of Florida. These InGaAs samples were epitaxially grown $In_{.53}Ga_{.47}As$ on a lattice-matched InP substrate.

Low-dose samples from IBM were ion-implanted to a sheet carrier density of $1x10^{14}$ cm^{-2} at an energy of 20 keV. High-dose samples from the University of Florida were either ion-implanted to a sheet carrier density of $5x10^{14}$ cm^{-2} at an energy of 10 keV, or grown using MBE with Si dopant concentrations of $1x10^{20}$ cm^{-3} Some samples from the University of Florida were already pre-annealed by RTA; these samples were used for the post-RTA annealing studies. All the University of Florida samples also

were capped with an additional 15 nm thick of Al_2O_3 capping layer. The effect of this capping layeris discussed in Appendix A.3. In concept, Al_2O_3 may potentially prevent arsenic leaving from the InGaAs surface during annealing [1].

Figure 2.3 provides a summary of the samples, their conditions, and the experimental annealing techniques used for each sample. The CO_2 laser spike annealing studied were performed over a range of dwell times from 250 µs to 2 ms while diode annealing studies were performed over a range of 5 -10 ms. We chose to use different laser sources, either the CO_2 laser or the diode laser, to anneal the various InGaAs samples depending on the substrate.

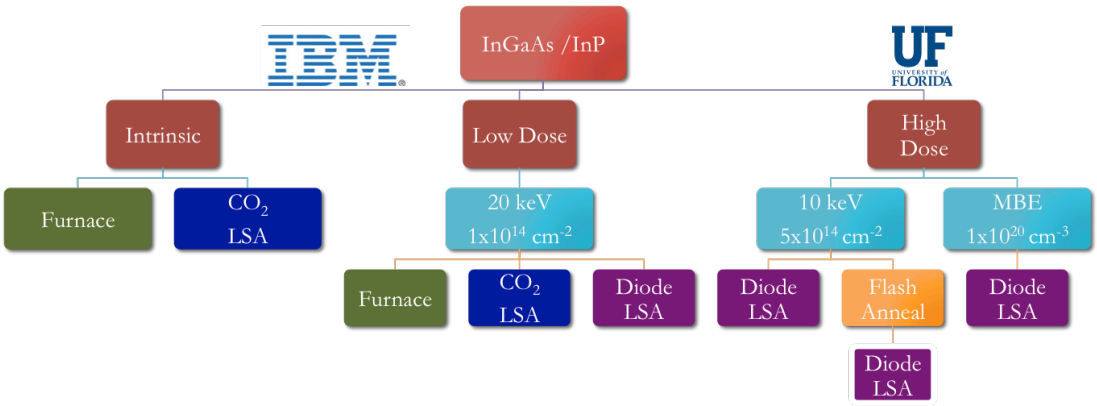

Figure 2.3: The schematic showing all the InGaAs samples which are used in this project with their doping conditions and the annealing techniques used to investigate them.

2.3.1 Samples Conditions

There were three types of intrinsic InGaAs wafers provided by IBM; two had been epitaxially grown on heavily doped InP substrates and one on semi-insulating InP substrates. These wafers were all diced into 6 x 6 mm samples for further examination and processing. Portions of these samples were sent back to IBM for silicon ion implantation. The dose was $1x10^{14}$ cm^{-2} with an energy of 20 keV. A schematic cross-section of the IBM samples is shown in Figure 2.4.

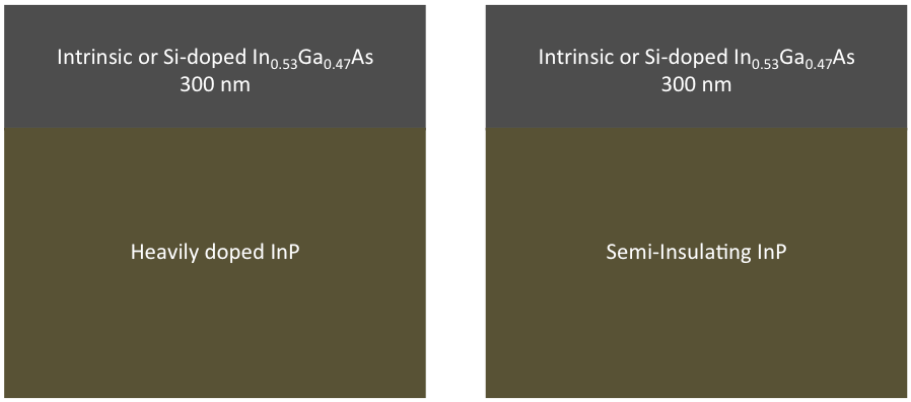

Figure 2.4: Schematic cross-section of the IBM Samples. InGaAs on heavily doped InP substrates (left) and InGaAs on the semi-insulating InP substrate (right).

The silicon implant profile for a dose of $1x10^{14}$ cm^{-3} with an energy of 20 keV was simulated using the TRIM program, as shown in Figure 2.5 [2]. The highest Si concentration is approximately 30 nm from the surface, which is comparable to the depth of the Raman spectroscopy probe (Chapter 3).

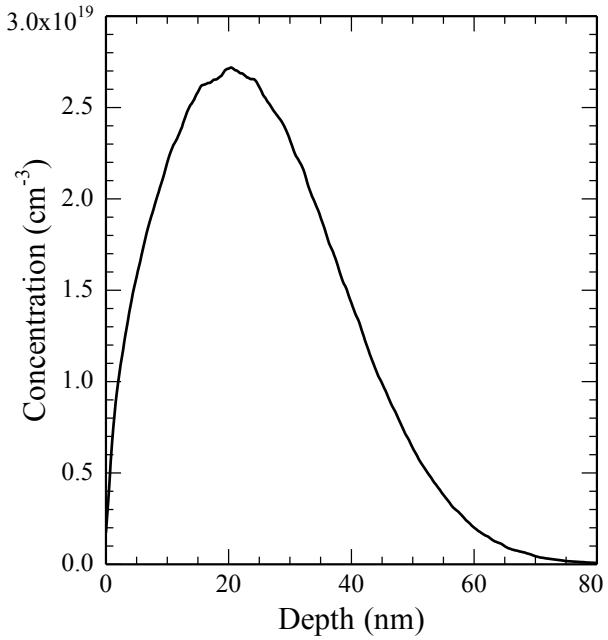

Figure 2.5: TRIM simulation of the concentration-depth profile of the IBM samples [2].

Samples containing higher silicon dopant concentrations were provided by Professor Kevin Jones, including Si^+ ion-implanted and molecular beam epitaxy (MBE) grown InGaAs on a semi-insulating InP substrate. The University of Florida ion-implanted samples were implanted at 80°C at a dose of $5x10^{14}$ cm^{-3} and at an energy of 10 keV. The MBE samples were grown with a dopant concentration of $1x10^{20}$ cm^{-3}. A schematic cross-section of the University of Florida samples is shown in Figure 2.6.

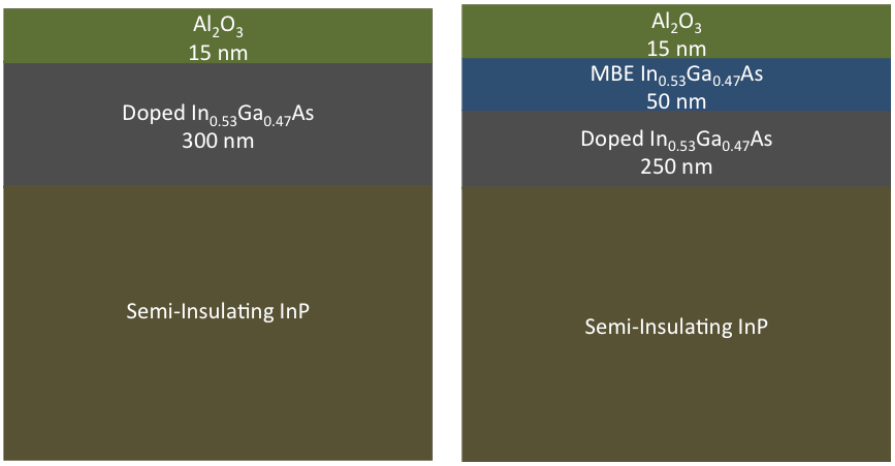

Figure 2.6: Schematic cross-section of samples from the University of Florida; 300 nm InGaAs layer epitaxial grown on the semi-insulating InP substrate (left) and 50 nm MBE grown InGaAs on top of the 250 nm InGaAs layer and the semi-insulating InP substrate (right). All the University of Florida samples were capped with a 15 nm Al_2O_3 layer to prevent film degradation during annealing process.

The MBE-grown doped InGaAs samples were grown layer by layer in the presence of the Si dopants, indium, gallium, and arsenic atoms, which were heated and injected from the effusion cells. Good quality Si^+-doped InGaAs films were condensed on the substrate at a slow rate compared with other deposition methods. This procedure results in an implant profile that is uniform throughout the MBE-grown layer.

There was an additional 15 nm capping layer of Al_2O_3 grown using atomic layer deposition (ALD) on each of the University of Florida samples. In order to study the effect of the capping layer on the InGaAs samples under laser spike annealing, a

similar Al_2O_3 capping layer was grown on some of the IBM samples at the University of Florida; results are shown in Appendix A.3.

2.3.2 Annealing Conditions

In this thesis, two types of annealing were studied, LSA and furnace annealing. A single scan annealing approach using LSA, without overlapping laser scans, resulted in a temperature gradient across the annealing, effectively allowing us to study the effect of rapid heating as a function of the peak temperature. In this way, LSA allows us to obtain detailed annealing information using a minimal number of samples. In contrast, it is more typical in industrial settings, for overlapping scans to be employed in order to create uniform thermal profiles. Studies employing overlapping scans of laser spike annealing will be needed for future work. As a comparison to the LSA, we explored longer time annealing behavior using furnace-annealing. More details on the furnace annealing are provided in section 3.5.

2.3.2.1 CO_2 Laser Spike Annealing

InGaAs, with a band gap of 0.75 eV, is transparent to the 120W far-infrared CO_2 laser (λ= 10.6 μm), consequently CO_2 annealing could be used with InGaAs samples sitting on heavily doped InP substrates. The heavily doped InP substrate is heated by the laser through free carrier absorption. This allows the InGaAs layer to reach thermal equilibrium with the InP substrate. Both intrinsic and Si^+-doped InGaAs IBM samples were annealed within a sub-millisecond time frame; from 250 μs to 2 ms dwells were used in this study.

The CO_2 laser was operated at 120 W and nominally focused to a FWHM 90 μm by 650 μm line beam with bi-Gaussian like profiles in both axes. The InGaAs layer is treated as being thermally thin. The laser beam on the sample was scanned over a velocity range of 40-400 mm/s. The beam profile of the CO_2 laser is shown in Figure 2.7.

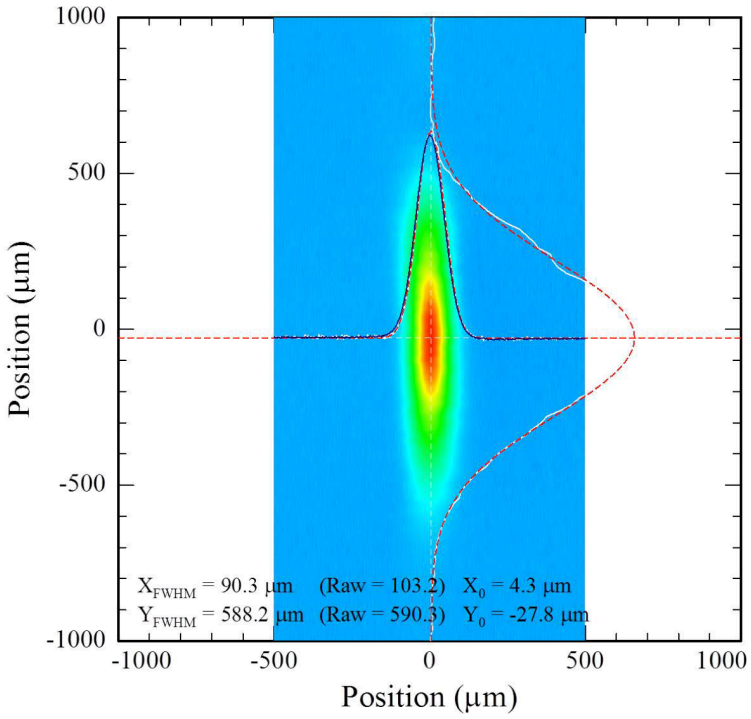

Figure 2.7: CO_2 beam profile in the x- and y- directions. The FWHMs of the x-direction is 90.3 μm and the y-direction is 588.2 μm. Both directions are Gaussian in shape. The center (red) is in hotter than outside (green and light blue).

2.3.2.2 Diode Laser Spike Annealing

For InGaAs on semi-insulating InP substrates, the near-infrared diode laser (λ= 980 nm) was used it couples directly with the InGaAs layer. These samples were annealed over a range of dwell times from 5 ms to 10 ms.

The diode laser was operated at 110 A and focused in an isosceles trapezoid in the long axis with a 1.5 mm flat top and 300 μm sides and a Gaussian shape with a FWHM of 300 μm in the short axis. The 5 -10 ms dwells explored in this thesis lead to scan velocities from 30-60 mm/s. The laser beam profile of the diode laser is shown in Figure 2.8.

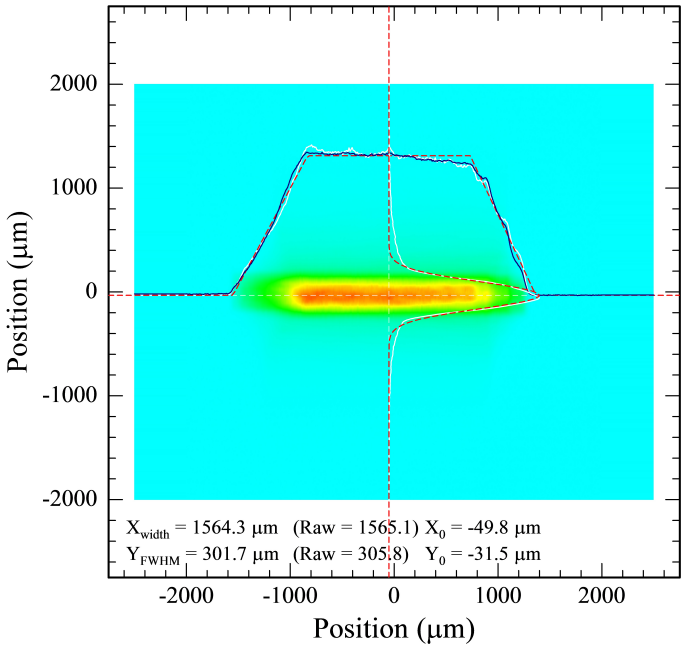

Figure 2.8: Diode beam profile in the x- and y- directions. The FWHMs of the x-direction is 1564.3 μm and the y-direction is 301.7 μm. The x- direction is in trapezoidal shape and the y-direction is roughly Gaussian.

2.4 LSA Thermal Calibrations

To quantitatively understand the difference between laser spike annealing and other annealing methods, it is critical to determine the absolute temperatures during processing. To do so, temperatures were calibrated using platinum thermistor measurements and polymer thermal decomposition. Thermistors resistivity relies on

the change in temperatures. Temporally and spatially resolved resistances were measured using thermistor and converted to temperature. In laser spike annealing, different annealing conditions (especially temperature) are accessed via changes to the laser power and dwell time. By probing resistance as a function of power and dwell during laser spike annealing, we are able to obtain quantitative temperatures for annealing.

Thermistor measurements were scaled to the known decomposition temperature of a polymer, yielding absolute temperatures. The polymer P(MAdMA-*co*-GBLMA) was used to calibrate the CO_2 thermistor data on InP substrate as it completely decomposes after exposed to LSA near 650 ^{o}C [3]. A layer of the polymer was spun on the InGaAs samples with initial thickness determined using profilometry or optical reflectance (filmetrics). Laser spike annealing was performed at different powers and dwells until polymer decomposition temperature was reached. Similar polymer decomposition experiments were also performed using diode laser spike annealing as well. More detail on the polymer decomposition experiment is given in section 2.4.2. Other photoresists such S1805 and S1813 were also used with similar results.

2.4.1 Pt Thermistor Calibrations

Thin film platinum resistors (thermistors) were fabricated on the surface of InGaAs. The thermistors measure the change of the resistance as a function of time and position on the moving sample. The temperature/resistance changes in direct proportional to the temperature on the surface of the sample. The resistances were

further converted to absolute temperature using the polymer decomposition calibrations.

Thermistor measurements were needed for both the CO_2 and diode lasers. Measurements for the CO_2 laser are complete which those for the diode laser remain in progress. In principle, the method to get the thermistor measurement is the same for both lasers. In this thesis, only the (completed) CO_2 thermistor measurements are discussed.

2.4.1.1 Design of Thermistors

The thermistor device layout is shown in Figure 2.9. A 30 Ω platinum resistor lies at the center of the 6 mm square device. There are six Ni contact pads that are wire-bonded to the platinum resistor. Detailed dimensions of the thermistor device are labeled in Figure 2.9. An optical image of the fabricated Pt thermistor is shown in Figure 2.10 with cross-sectional schematic shown in Figure 2.11. A four-point Kelvin probe-like structure was designed to measure the resistance to minimize errors from parasitic resistances.

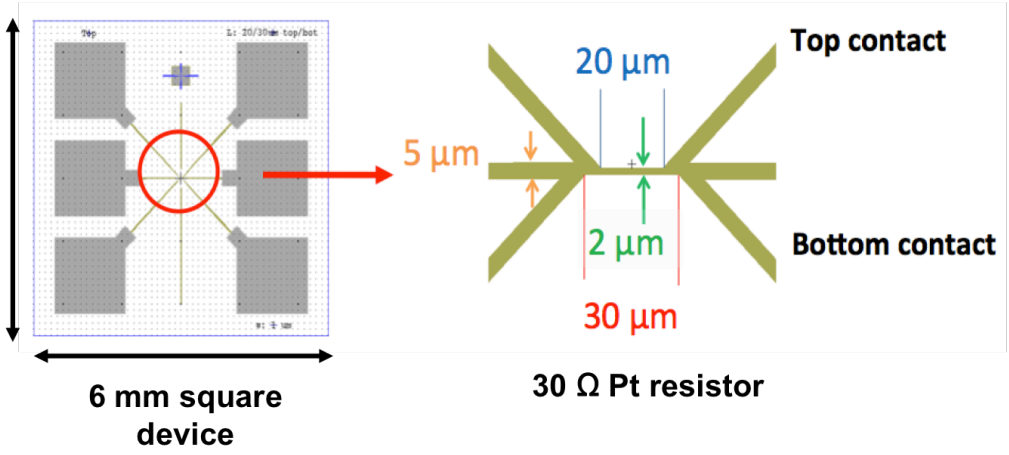

Figure 2.9: Thermistor device layout is shown on the left. The six gray squares are the contact pads. The lines in the middle are Pt thermal resistor wires. The image on the right shows the detail of the thermistor itself. The specific dimensions are labeled on the right graph.

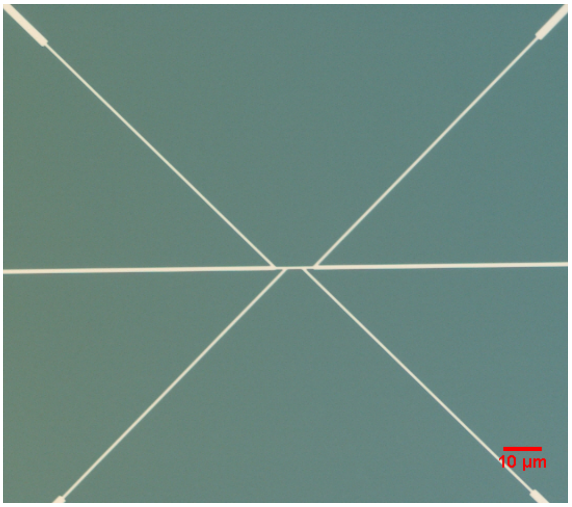

Figure 2.10: Optical image of the fabricated thermistor. The scale bar is 10 μm.

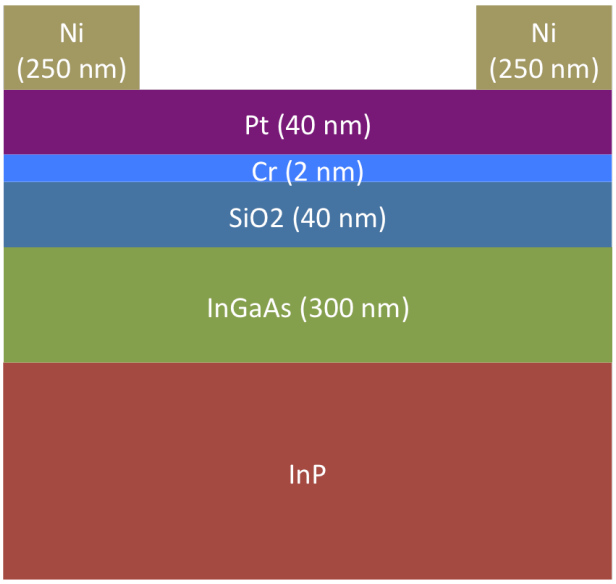

Figure 2.11: Schematic cross-section of the thermistor: 40 nm Pt resistor with 2 nm Cr adhesion layer, 40 nm insulation layer and 250 nm of Ni for the contact pads.

2.4.1.2 Thermistor Mechanism

The measured spatial temperature profile (orthogonal to the scan direction) is shown in Figure 2.12 with overlays of the Gaussian fit used for position to temperature conversions. Along the lateral direction of the laser beam, the spatial profile exhibits near a Gaussian like shape, but is slightly asymmetric due to the incident laser beam incident at an angle off-normal to the sample.

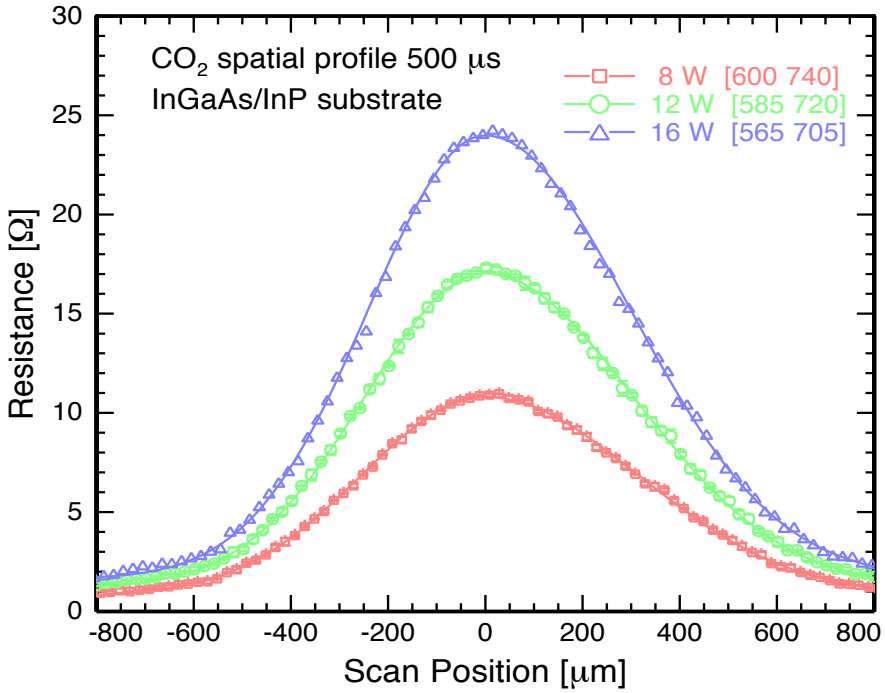

Figure 2.12: Spatial profile for a 500 μs dwell at different values of the laser power under CO_2 LSA. The increasing power provides higher temperature to the sample, resulting in higher resistance changes to the Pt thermistor. The peak temperature for 16 W is approximately twice that of the 8 W conditions.

The relationship between device resistance change and temperature is given by equation 2.1, assuming the thermal coefficient of resistivity (α) constant in the annealing temperature range, here R_t is the resistance of the Pt wire at specific annealing temperature. R_o is the resistance of the Pt wire at room temperature. α is the thermal coefficient of resistivity [4]. As the annealing temperature is increased, the resistances of the Pt wire increases as well.

$$R_t = R_o(1 + \alpha(T(t) - T_o)) \qquad (2.1)$$

2.4.2 Absolute Temperature Calibration

With the photoresist spun onto the InGaAs sample, laser scans were run on the resist-coated samples at various values of the power and dwell. At a critical temperature, films began to decompose until finally disappears at some higher temperature. The thickness and width of the polymer decomposition were determined using profilometry or optical reflectance, as well as visually. Different polymers provide different scaling points for the thermistor measurements. As an example, at 1 ms dwell and 19 W of power, the photoresist P(MAdMA-*co*-GBLMA) completely decomposed corresponding to a temperature of 650 ^{o}C.

2.4.2.1 Design

A schematic of the polymer decomposition calibration graph after laser spike annealing is shown in Figure 2.13. The polymer shows some color change when first exposed to the laser beam as it thermally activates the photoresist. The chemistry of the polymer changes more dramatically after heat treatment. Once the decomposition temperature is reached, the polymer begins to reduce in thickness and the width of the ablated region concomitantly increases. We consider the decomposition temperature to be reached when the polymer has been completely removed following particular LSA condition.

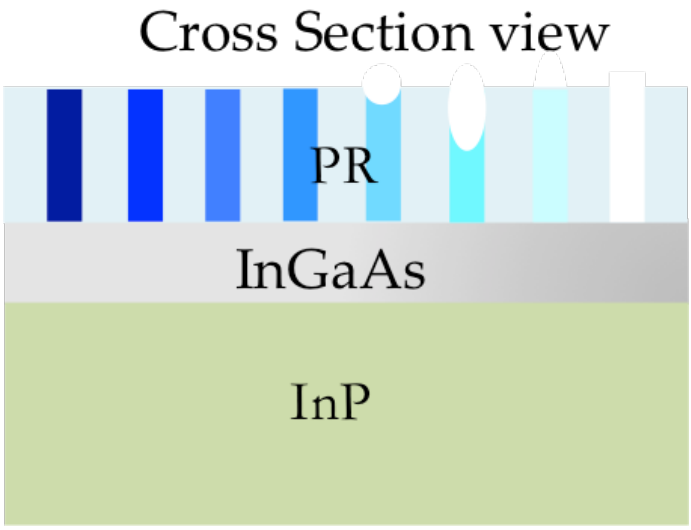

Figure 2.13: Schematic of polymer decomposition calibration after LSA. For the photoresist layer, the annealing temperature increases from left to right. The polymer first is activated by laser power and slowing decomposes with increasing annealing temperature.

An optical image of a polymer on InGaAs film after LSA exposed at varying annealing conditions is given in Figure 2.14. Temperatures from left to right across the sample. The center of each stripe is annealed at a highest temperature at the specific LSA condition.

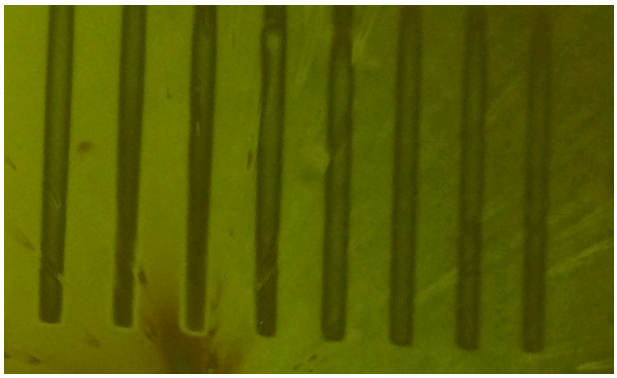

Figure 2.14: Optical image of an S1815 polymer film after LSA. From the left to right, the photoresist get annealed at higher laser powers. As a consequence, the centers of the annealing region (white) get wider with the increasing laser temperature.

As a example, the profilometer measurements for polymer decomposition at 250 μs using CO_2 laser spike annealing at estimated temperatures from 1000 ^{o}C to 1200 ^{o}C on Si substrates are shown in Figure 2.15. The polymer S1805 is observed to fully decompose at 1100 ^{o}C with deep trenches and wide stripe (green), partial decomposition of polymer at 1000 ^{o}C shown (red). As the annealing temperature exceeds the polymer decomposition temperature, the width of the polymer decomposition region increases until the center reaches 1200 ^{o}C (blue).

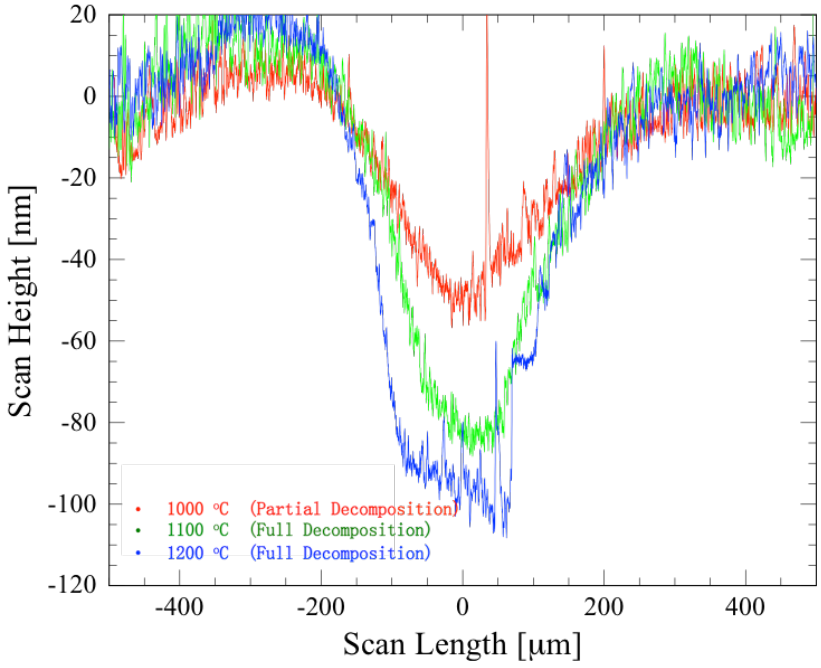

Figure 2.15: Profilometer measurement of polymer decomposition at 250 μs for S1805 decomposition on Si. Red curve shows partial decomposition at 1000 °C. Green curve shows onset of full decomposition with center reaching 1100 °C. Blue curve shows full decomposition with the center reaching 1200 °C.

2.4.3 Thermal Calibration Results

Similar polymer decomposition experiments were performed on InGaAs substrate using P(MAdMA-*co*-GBLMA) with a decomposition temperature near 650 °C. The decomposition conditions under different annealing conditions from 250 μs to 2 ms are summarized in Table 2.1. With these polymer decomposition conditions, the spatial profile at different powers and dwells are calibrated to absolute temperature under laser spike annealing. The relationship between peak annealing temperature and specific laser power at different dwells is shown in Figure 2.16. For each dwell, the

power was ramped up from zero to a desired power and then ramped down to low temperature during the thermistor measurement. Equipping both thermistor and polymer calibrations, the correlation of position and temperature is obtained. By knowing the distance away from the center of annealing, temperature under LSA can be estimated by using the temperature spatial profile as shown in Figure 2.17. It is extremely useful for the further analysis on Raman characterization (Chapter 3) and Electrical characterization (Chapter 4) under LSA.

Table 2.1: The CO_2 LSA polymer calibration at different dwells and powers using P(MAdMA-*co*-GBLMA) decomposing at 650 °C .

Dwell	250 μs	500 μs	1 ms	2 ms
~650 °C	~30W	~24W	~19W	~17W

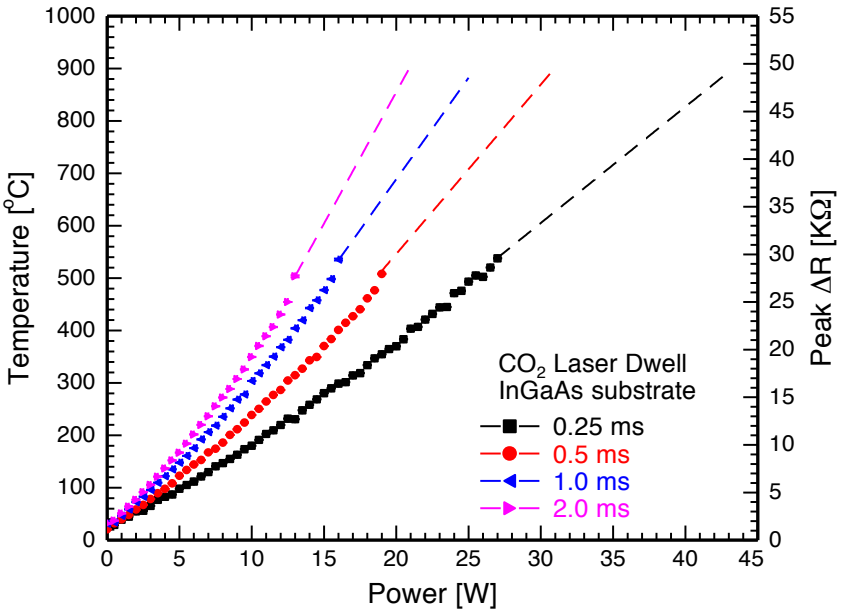

Figure 2.16: Calibration curves for thermistor measurements under LSA using CO_2 laser at different dwells. The specific power is plotted in x axis for each dwell with corresponding annealing temperatures on the left axis and resistances on the right axis.

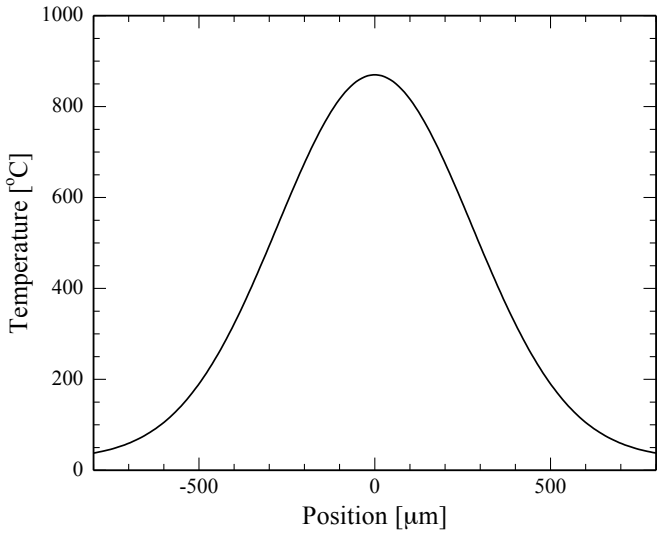

Figure 2.17: Temperature spatial profile at 1 ms dwell and 24W annealing power under CO_2 LSA. The peak temperature at center is ~850 ^oC and cooler away from either side.

REFERENCES

[1] Penna, Thereza, B. Tell, A. S. H. Liao, T. J. Bridges and G. Burkhardt. "Ion implantation of Si and Se donors in $In_{0.53}Ga_{0.47}As$." *Journal of applied physics* 57.2 (1985): 351-354.

[2] Ziegler, James. "Interactions Of Ions With Matter." Web

[3] Jung, Byungki. "Laser-Induced Millisecond Heating Of Polymers And Small Molecules For Pattern Development." Ph.D thesis, Cornell University, (2014).

[4] Iyengar, Krishna, Byungki Jung, Michael Willemann, Paulette Clancy and Michael O. Thompson "Experimental determination of thermal profiles during laser spike annealing with quantitative comparison to 3-dimensional simulations." *Applied Physics Letters* 100.21 (2012): 211915.

CHAPTER 3

RAMAN CHARACTERIZATIONS

3.1 Backgrounds of Raman Spectroscopy

Raman spectroscopy is a powerful tool to investigate vibrational and phonon excitations properties of materials. In this work, we use micro-Raman spectroscopy extensively to understand structural modifications after LSA.

Raman spectroscopy, a non-destructive optical technique, measures inelastic energy changes when a photon excites an electron from one state to a virtual energy state, which subsequently relaxes to a different state. Monochromatic laser light illuminates the samples as shown in Figure 3.1 and inelastically scattered photons are detected by a high-resolution spectrometer. Since it can identify individual vibrational modes corresponding to given characteristic molecular motions in the sample, Raman is a good method to "fingerprint" of the sample. For our purposes, it is important that Raman has been shown to be a sensitive measure the crystalline quality, carrier concentration, defects, microstructure and stress in the sample.

3.2 Molecular Mechanisms Affected by Raman Spectroscopy

In this work, Raman spectroscopy has been used to characterize InGaAs following Si^+ implantation and annealing. As shown in Figure 3.1, incident photons at wavelength λ_i illuminate a material. Most of the light is scattered elastically with no change in the wavelength (Rayleigh Scattering), however a small fraction of the light that is scattered inelastically with a different wavelength to λ_i (Raman scattering). The

energy difference corresponds to excitation of a phonon in the sample. This makes Raman spectroscopy is a sensitive probe of vibrational states and hence the structure of the material. In Stokes Raman scattering, photons lose energy to the crystal; photons that gain energy from the phonon system are referred to as anti-Stokes Raman scattering.

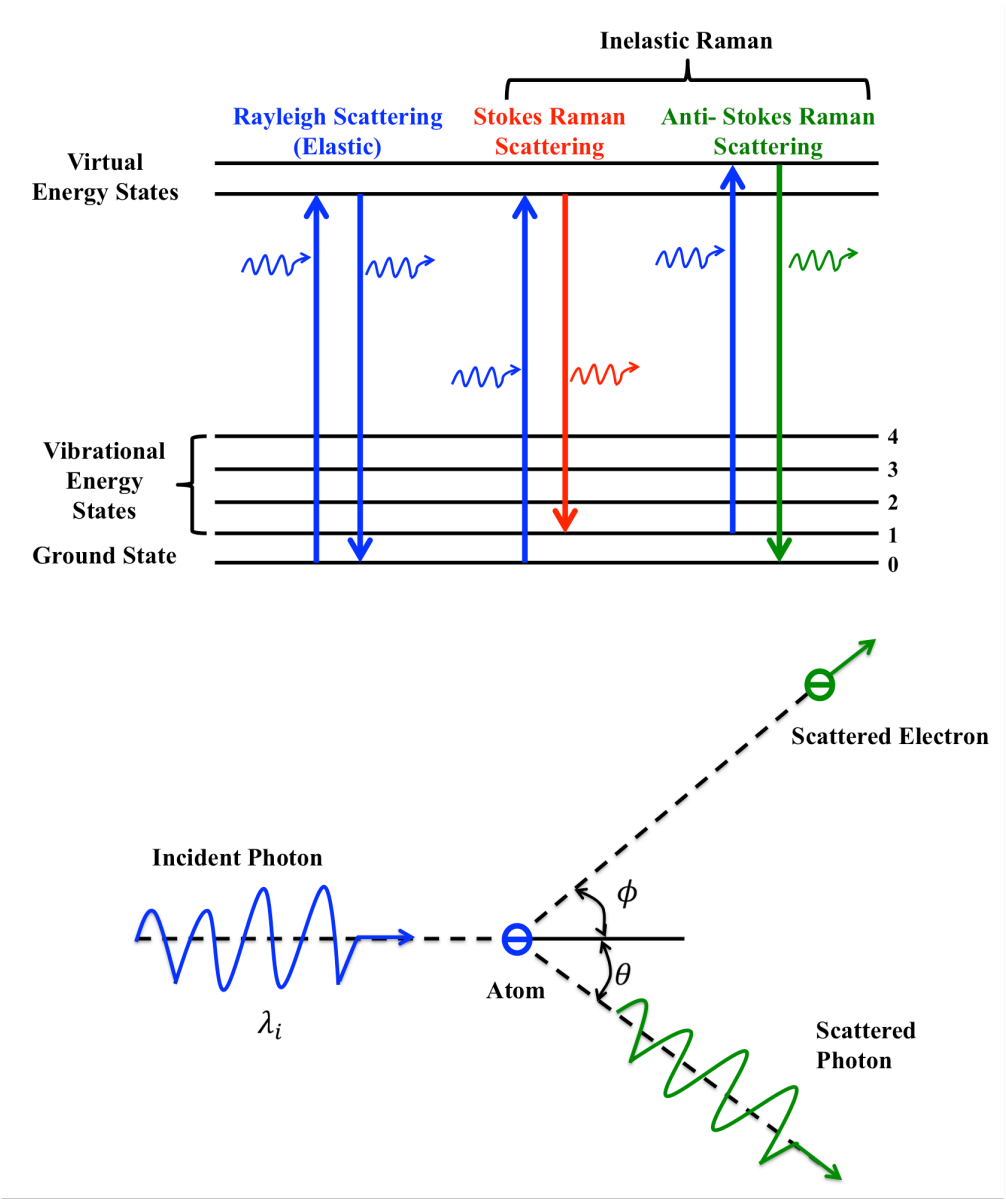

Figure 3.1: Principles of Raman scattering

The Raman intensity is also directly proportional to $(1/\lambda)^4$, favoring short wavelengths for the highest signal; however, shorter wavelengths are more strongly attenuated resulting in shallower probe volumes. Wavelengths and photon energies of Raman lasers used in this work are given in Table 3.1.

Table 3.1: Laser sources used in Raman measurements and the associated photon energies. The majority of this work was done with the 488 nm source.

Wavelengths λ [nm]	**Energy [eV]**
488	2.541
532	2.33
785	1.579

Figure 3.2 shows a schematic of a micro-Raman spectroscopy set-up. The incident laser first passes through a series of filters and reflects from the samples, and Raman shifted photons are detected via a CCD camera.

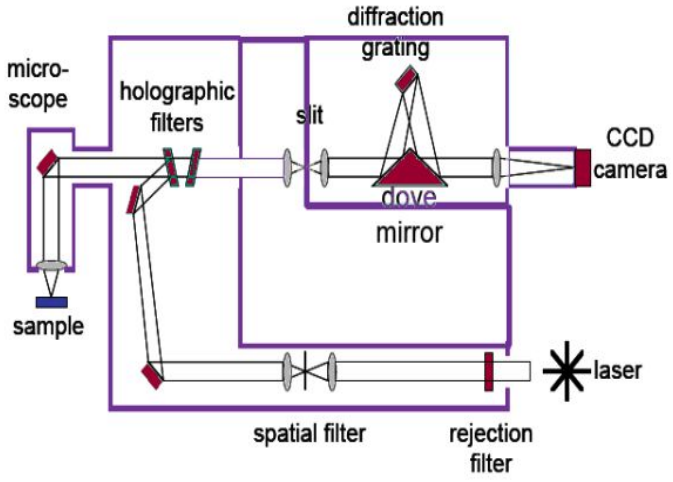

Figure 3.2: A typical Raman set-up

All Raman measurements were taken using a Renishaw Raman spectroscopy system in the Cornell Center for Materials Research (CCMR) facilities. Laser sources at 488 nm and 532 nm were used in different contexts in this thesis. Earlier work had shown strong fluorescence using the 785 nm laser source for InP substrates, which limited detection of the necessary peaks [1]. In order to minimize fluorescence, the majority of this work used the 488 nm source.

Laser exposure time on the sample and the number of accumulations also affect the signal/noise ratio. Long exposure times and multiple accumulations to achieve adequate sensitivity are generally required. For these studies typically 3 s exposure time and 4 accumulations was used, otherwise specified.

The micro-Raman microscopy has a spatial resolution near 1 μm, however the penetration depth into the samples depends on the incident laser wavelength, as given in Table 3.2 and Equation 3.1 where δ_p is the penetration depth, k is the extinction coefficient, α is the attenuation constant.. The extinction coefficient, k, for InGaAs is around 1 [2]. Shorter wavelength hence gives rise to a more surface sensitivity.

$$\delta_p = \frac{1}{\alpha} = \frac{\lambda}{4\pi k} \qquad (3.1)$$

Table 3.2: The penetration depth (δ_p) for different wavelengths (λ) of Raman laser [3]. Longer wavelengths laser leads to deeper penetration into the sample.

Wavelengths λ [nm]	**Penetration depth δ_p [nm]**
488	38
532	42
785	62

3.3 Typical InGaAs Raman Spectrums

InGaAs is a ternary compound semiconductor alloy, exhibiting behavior of both InAs and GaAs. A typical InGaAs spectrum is shown in Figure 3.3. For InGaAs, there are several characteristic peaks corresponding to the InAs longitudinal optical (LO), GaAs LO, disorder peaks R*, GaAs transverse optical (TO) and InAs TO peaks. Depending upon the crystal orientation and experimental geometry, some of these peaks may be optically forbidden, such as the TO peaks. The InAs-like LO phonon mode was observed at 232 cm^{-1} and the GaAs-like LO phonon mode at 269.5 cm^{-1}.

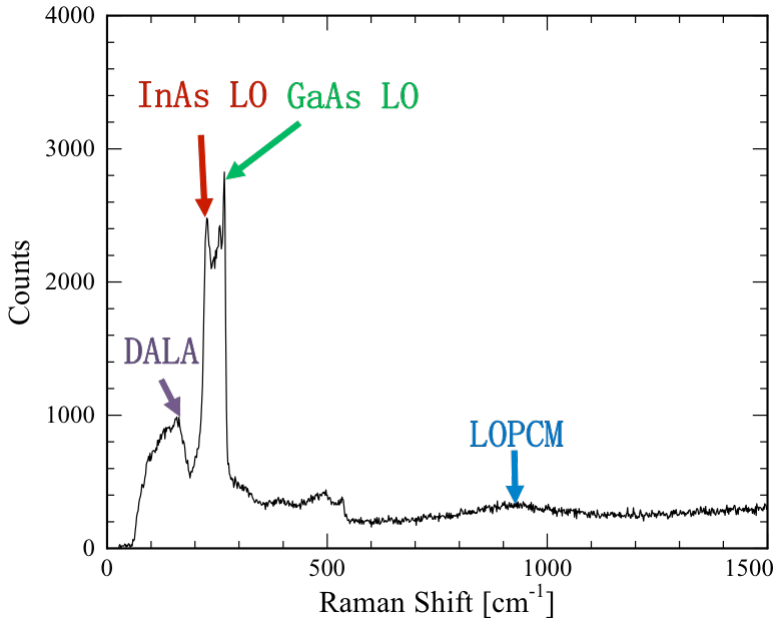

Figure 3.3: The typical InGaAs Raman Spectrum showing the location of the DALA (purple), InAs LO (red), GaAs LO (green) and LOPCM (blue) peaks.

The position of the longitudinal optical phonon plasmon coupling mode (LOPCM) Raman shift correlated with the average peak active carrier density as obtained from Hall measurements [6]. In contrast to the sheet conductivity measurements, which depend on the carrier density and the mobility, the LOPCM peak allow us to measurement directly the active carrier concentration within the volume of sample probed by Raman. Figure 3.4 shows the position of LOPCM peak as a function of carrier density, these data was used determine carrier activation after LSA.

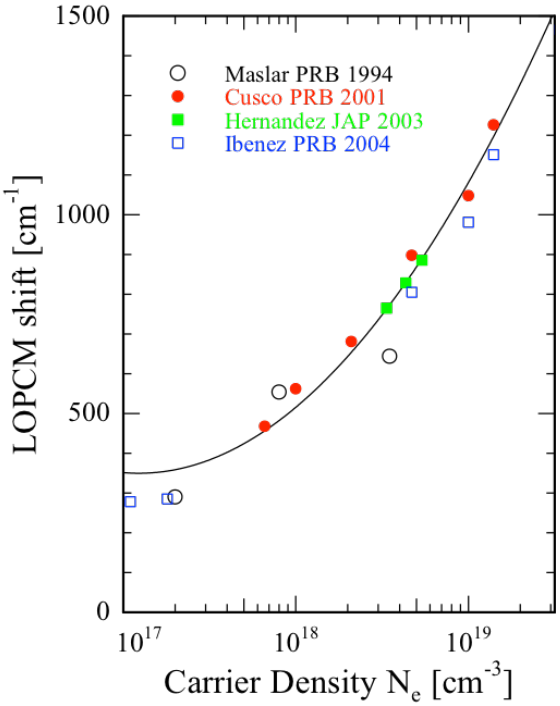

Figure 3.4: LOPCM peak position as a function of active carrier density.

The area of the GaAs LO phonon peaks was used to quantify the crystalline quality in intrinsic samples, and to determine the onset of substantial carrier activation in extrinsic samples. The peak position and peak information are shown in Table 3.3. As LSA thermally activates carriers, inelastically scattered phonons can also couple with a plasmon resulting in a reduction of the GaAs LO phonon mode and a concomitant rise in the LOPCM peak. The LOPCM peak is located between 600-1500 cm^{-1} and is a critical peak for this work. The LOPCM peak position can be used to quantify the active carrier density, which will be shown in Figure 3.4.

Table 3.3: Key Raman peaks of InGaAs [5]

Peaks	**Peak Position [cm-1]**	**Allowed Modes in (100)**
InAs LO	238	Yes
GaAs LO	290	Yes
R*	244	Yes
InAs TO	229	Forbidden
GaAs TO	270	Forbidden

The broad band observed 100 cm^{-1} and 200 cm^{-1} corresponds to intrinsic alloy disorder (DALA) modes. Peaks between 430 cm^{-1} and 550 cm^{-1} are associated with the second-order optical Raman spectrum, such as that located around 535 cm^{-1} which corresponds to the GaAs-like 2LO mode [4].

In Si-implanted samples, the GaAs primary LO phonon mode is a good indication of film quality until dopants are activated. At higher concentration, the secondary LO phonon mode becomes a better probe as the long wavelength LOPCM mode does not interfere with the second-order optical peaks [*5*].

Silicon introduced into InGaAs samples by ion implantation. During implantation, atoms are accelerated and bombarded into the InGaAs lattice. As a result, the crystal is damaged and potentially amorphized as energetic ions displace In, Ga and As atoms. Implanted atoms may also come to rest in interstitial sites, instead of substitutional sites. Ion implantation thus defects that most be eliminated by a suitable annealing process.

Figure 3.5 shows Raman spectra for before and after ion implantation. Due to defects introduced during implantation, the shoulder band at 300 cm^{-1} to 550 cm^{-1} and the GaAs LO peaks at 269.5 cm^{-1}, these peaks are all decrease in intensity and confirm the implant damage.

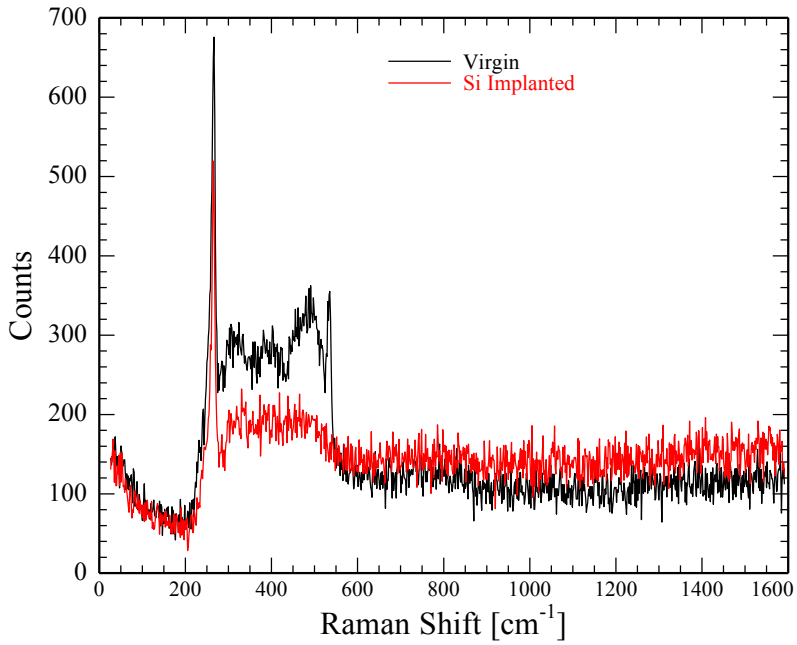

Figure 3.5: InGaAs spectra before (black) and after (red) Si implantation. The crystal quality is lost as indicated by the loss of the peaks at 300 – 500 cm^{-1}.

3.4 The Filter Effect of Raman System

Most Raman analyses were performed using the 488nm laser source. However, the 488nm Rayleigh filter had degraded over the years, resulting in a much higher cut-off wavenumber. Peaks below 200 cm^{-1} are strongly imparted by this filter. Figure 3.6 shows the filter response for the old 488 nm filter and a 532nm filter. The 488 nm filter is opaque below 200 cm^{-1} while the 532 nm filter remains transparent to 100cm^{-1}.

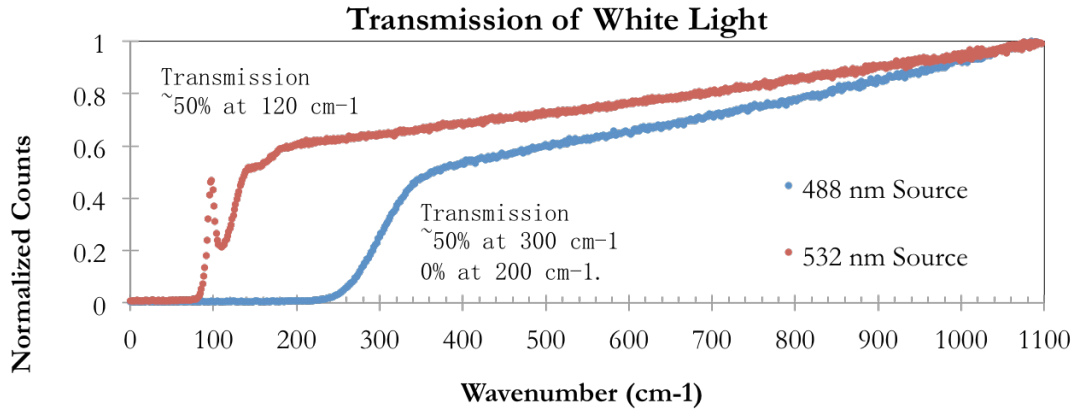

Figure 3.6: White Light Transmission Study for Raman Filter Cut-off for both 488nm Raman system and 532nm Raman system before the filter changes. The 488nm Raman signal before 200 cm^{-1} get completely blocked out while the 532nm Raman still maintain good signals.

During this project, the 488 nm filter was replaced as shown in Figure 3.7. With the old filter, only a portion of the GaAs-like LO modes was observed. The replacement filter clearly shows the disorder-activated longitudinal acoustic mode (DALA) modes and the InAs LO modes. Fortunately, the key LOPCM peak is above 250 cm^{-1} and hence was not directly affected.

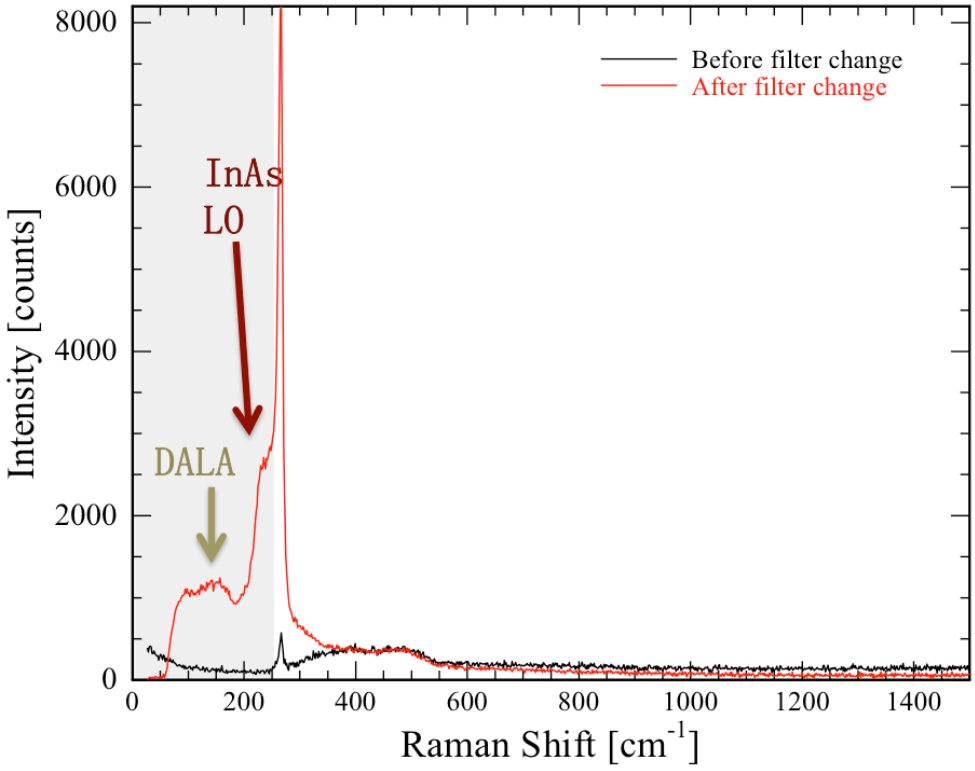

Figure 3.7: The InGaAs spectrum before and after the filter was changed using the 488nm laser. Before filter changes, the filter completely blocks the signals from DALA modes.

For our purposes, two of the most important peaks in the InGaAs spectrum are the GaAs LO peak and LOPCM peak, both at energies above 250 cm^{-1}. After replacing the filter, the Raman spectrum overall was stronger resulting in reduced noise level. Some samples were also analyzed using 532 nm source.

3.5 Furnace Annealing of The Low Dose Samples

In order to compare the effectiveness of LSA, several low dose IBM samples were furnace annealed in an inert environment for 15 minutes at temperatures up to 750 ^{o}C.

Raman spectra from the furnace annealed samples are shown in Figure 3.8. The film quality improves at 450 ^{o}C as indicated by the characteristic primary and secondary InGaAs phonon peaks. At high temperature (> 600 ^{o}C), dopant activation become significant as the LOPCM peaks shifted to the right as increasing annealing temperature.

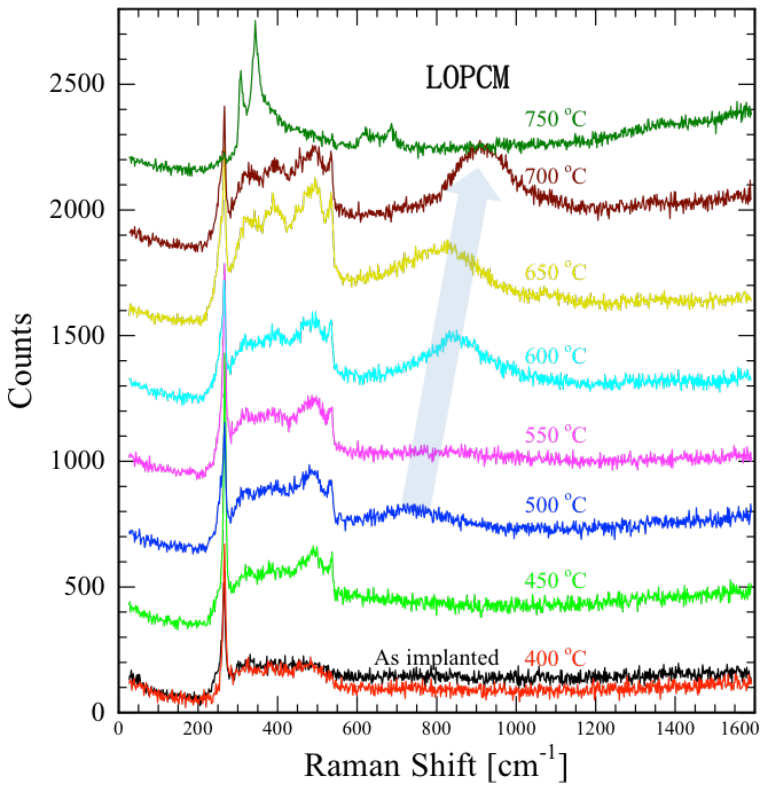

Figure 3.8: Raman spectra of furnace annealed InGaAs from 400 to 750 ^{o}C. The LOPCM peak gradually shifts to the right with temperature showing until the onset of damage at 750 ^{o}C (green).

Initial activation of Si appears near 600 °C with the LOPCM peaks appearing near 650 cm^{-1} - 800 cm^{-1} band with increasing temperatures. The LOPCM peak is shifted further to the right reaching maximum near700 °C at 910 cm^{-1}. We observed damage above 750 °C with loss of the characteristics InGaAs peaks. A signal arising from the InP substrate also appeared at this point, indicating loss of film integrity. The highest LOPCM shift corresponds to an estimated carrier density of $5.6x10^{18}$ cm^{-3}. Table 3.4 provides a summary of conditions associated with each furnace annealing temperature.

Table 3.4: Summary of furnace annealing outcomes at different temperatures

Temperature	**Condition**
400°C	Onset of film improvement
600°C	Initial activation of Si dopants
700°C	Peak activation of Si dopants
750°C	Onset of damage due to arsenic loss in the uncapped samples

3.6 LSA of The Low Dose IBM Samples

Corresponding Raman spectra of Si^{+} doped InGaAs samples following LSA are shown in Figure 3.9. These Raman spectra were used to determine the onset of dopant activation and the peak dopant activation. As the annealing temperature increased, the

GaAs LO peak increased in intensity, indicating annealing of ion implantation defects generated from the ion implantation process. As carriers were activated at higher temperatures, the GaAs LO peak dropped in magnitude as LO phonons coupled with the plasmon excitation. At the highest carrier densities, the GaAs LO phonon peaks almost completely disappeared.

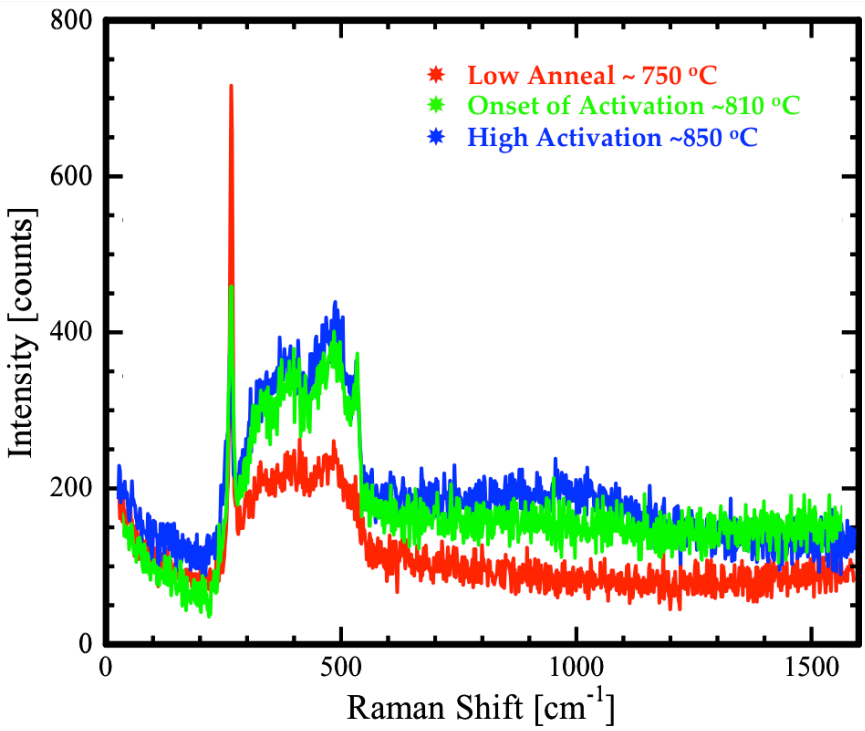

Figure 3.9: Film Quality As Indicated From The Shoulder Peaks at the onset of annealing (red), the onset of dopant activation (green) and the high point of dopant activation (blue).

Secondary peaks are also good indicators of film quality following LSA. These peaks remained fairly constant until the point of damage. The levels of the second-order peaks (shown by the black dashed line in Figure 3.9) did not change once the initial damage is removed by relatively low temperature anneals. From onset of dopant

activation to the highest point of this activation, the secondary LO phonon peaks remain constant in the shoulder band, showing that good film quality has been preserved during dopant activation. The drop in GaAs LO peak is a result of plasmon coupling into the LOPCM.

At temperature above 800 ^{o}C, the LOPCM peak becomes visible in the spectra indicating significant carrier activation. We fit the data to a Lorentzian lineshape using the Genplot program, as shown in Figure 3.10 [7].

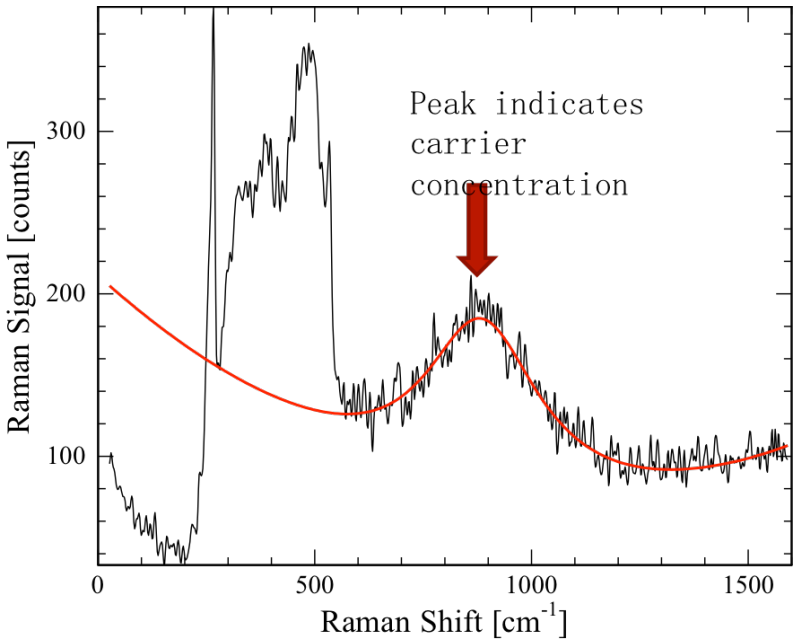

Figure 3.10: Extraction of the LOPCM peak position via a Lorentzian lineshape fit

Since the LOPCM peak was used to determine carrier activation in the sample, it was critical to carefully analyze these peaks. Both the peak area and the peak position of LOPCM show similar trends across the LSA annealing region as shown in Figure

3.11. Since the highest annealing temperature occurs at the center of the stripe, the center becomes damaged first for annealing temperature above the damage threshold. The highest peak area and highest peak position of LOPCM occur around -60 μm and 60 μm from the center. With LOPCM peak area and peak location following similar trends, inside the damage region, the peak area drops to zero and the position can not be reliably established. Indeed, the LOPCM peak is effectively not presented in this damaged region. The maximum dopant activation (based on the LOPCM Position) occurs at 950 cm^{-1}, approximately 65 μm away from the laser center.

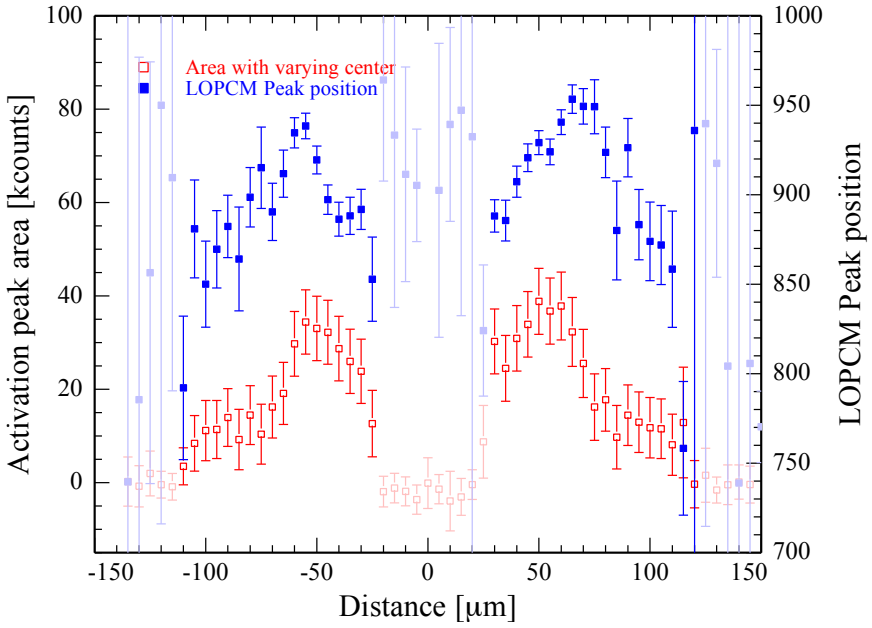

Figure 3.11: LOPCM peak area (left axis; corresponding points shown in blue) and peak positions (right axis; corresponding points shown in red) as a function of distance across the sample after a 1ms LSA at 24W annealing power. The peak temperature under these condition is ~870 ^{o}C.

The GaAs LO peaks correlates with film quality after LSA. Figure 3.12 shows the correlation between the GaAs LO and the LOPCM peaks. The GaAs LO initially increased with temperature (from 150 μm to 130 μm). At the onset of carrier activation, the LO peak couples with the plasmon, as observed in the region from 130 μm to 80 μm. As LOPCM intensity increase, the GaAs LO phonon peaks concomitantly decreases. The GaAs LO and LOPCM peaks both drop into zero at the damage threshold. The Raman observed damaged region matches well with the onset of visible damage as seen in the background of the Figure 3.12.

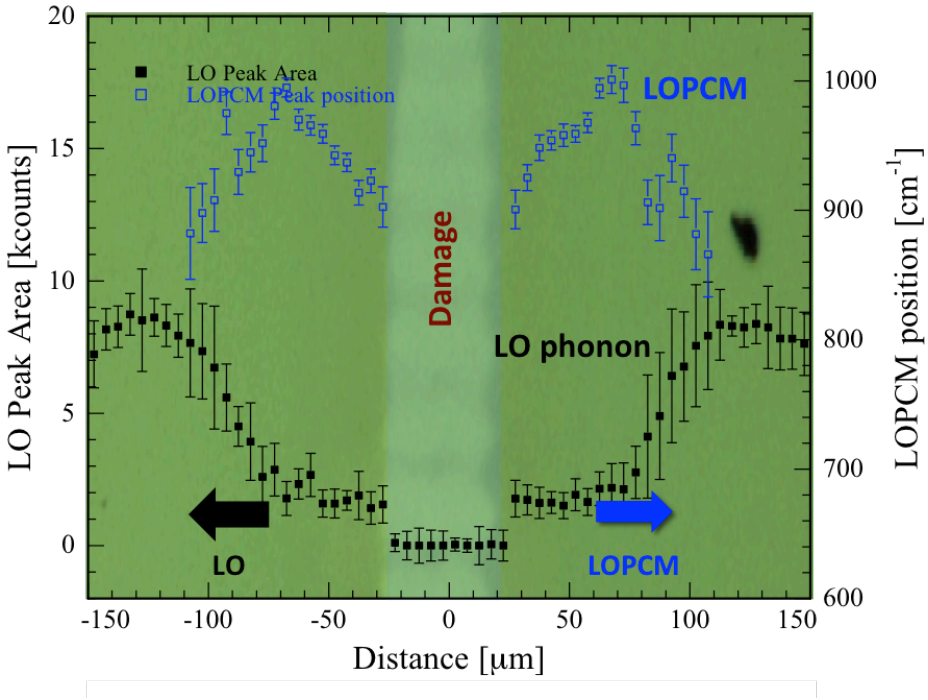

Figure 3.12: LO peak area (black) and LOPCM peak position (blue) as a function of position on the sample. The background is an optical microscopic image of the sample after LSA. Annealing beyond the damage threshold results in readily visible stripe in the center.

Using spatial profiles shown (Figure 2.17) and the maximum temperature, sample position after LSA can be converted directly to temperatures. Figure 3.13 shows the GaAs LO peak area and LOPCM peak position as a function of the peak according to temperature. Data on either side of the stripe center agree well with this conversion. The peak activation occurs at 850 ^{o}C with only 50 ^{o}C annealing window. Annealing beyond 870 ^{o}C damages the samples in the samples. Figure 3.14 shows the LO peak area and the LOPCM peak area correlation as function of temperature with similar conclusions.

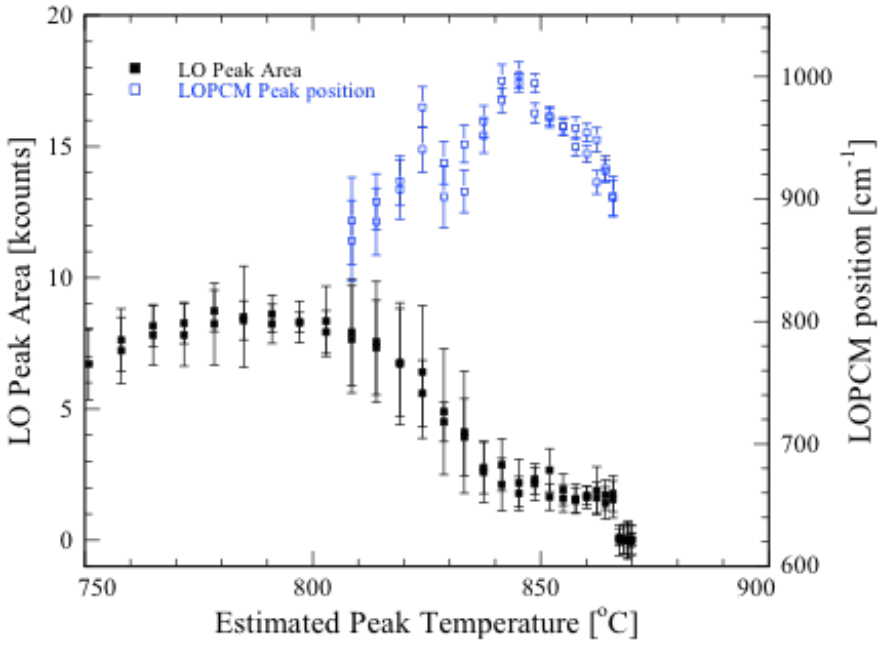

Figure 3.13: LO peak area (black) vs. LOPCM peak position (blue) as function of the peak annealing temperature.

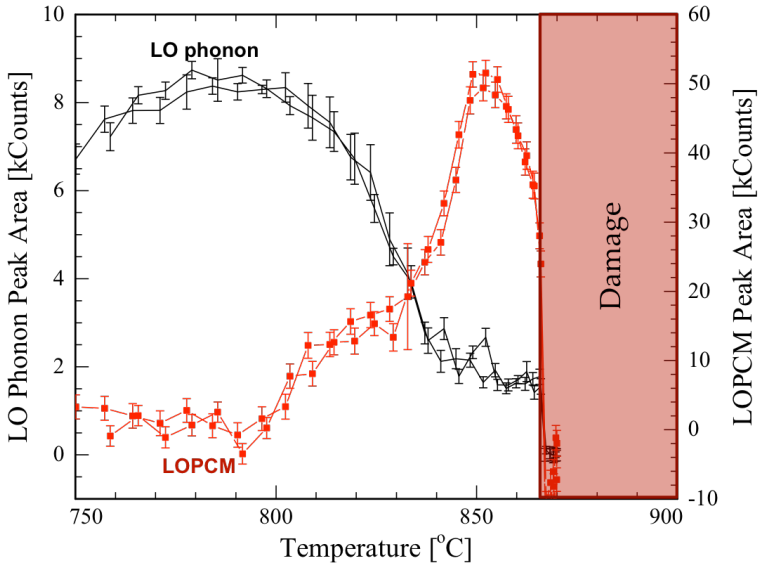

Figure 3.14: LO peak area (black) and LOPCM peak area (red) as function of the peak annealing temperature

For low dose implants with no capping layer, the damage threshold t occurs near 850 °C for laser spike annealing under CO_2 irradiation. Compared to furnace annealing for 15 min, the damage threshold is increased by ~100 °C - 150 °C. Damage thresholds for various annealing condition are shown in Table 3.5.

Table 3.5: Damage threshold table for low dose samples. LSA annealing was with a CO_2 laser source

Dwell	**Furnace**	**250 µs**	**500 µs**	**1 ms**	**2 ms**
Power (W)	N/A	42	30	24	18
Temp Estimate (°C)	700	>820	857	865	>785

Table 3.6 shows that the dopant activation for the low dose samples estimated from the LOPCM peak position. LSA improves the dopant activation, comparing with traditional thermal annealing method from $5.0x10^{18}$ cm^{-3} to $8.0x10^{18}$ cm^{-3}.

Table 3.6: Maximum dopant activation at varying dwells for low dose samples

Dwell	**Furnace**	**250 µs**	**500 µs**	**1 ms**	**2 ms**
LOPCM Peak Position (cm^{-1})	910	965	980	1000	970
Estimated Carrier Density (cm^{-3})	$5.0x10^{18}$	$6.0 x10^{18}$	$6.5x10^{18}$	$8.0x10^{18}$	$6.4x10^{18}$

3.7 LSA of High Implant Dose Samples

Samples implanted with a high dose of Si^{+} from the University of Florida, were also annealed by LSA. These samples were investigated to determine if activation depend on the concentration or only on the annealing temperature.

All samples from University of Florida were capped with a 15 nm Al_2O_3 layer. These samples were annealed using the 980 nm diode laser with a 5 ms dwell; the 980nm laser was required since samples were grown of semi-insulate InP substrates

Three types of samples were obtained from University of Florida: The first were implanted with a Si dose of $5x10^{14}$ cm^{-2}, at 10 keV and at 80 ^{o}C. Based on University of Florida studies of implant condition, implants at 80 ^{o}C produced the highest levels of dopant activation in InGaAs. The second type of samples were MBE-grown InGaAs with silicon dopant concentrations of $10x\ 10^{20}$ cm^{-3}. For MBE-grown

samples, the silicon was activated during film deposition with high metastable activation level. A third set of samples were pre-annealed, implants similar to the first set. Pre-annealing conditions involved either a 750 °C spike anneal or a 5 s fast ramp anneal. Laser spike annealing was on all of these sample types.

3.7.1 LSA of the Ion Implanted High Dose Samples

Figure 3.15 shows Raman spectra of high dose samples after diode LSA at a dwell of 5 ms and 75A current. With increasing temperature, the film quality improves as shown by increases in the GaAs LO peak and peaks between 300 to 500 cm^{-1}. As carriers are activated, the LOPCM peak shifts from 1000 $^{-1}$ to 1200 cm^{-1}. The peak carrier density, estimated from the 1200 cm^{-1} LOPCM peak position was $1.4x10^{19}$ cm^{-3}. Compared to the low dose implants, an increase in implant dose by a factor of 5 increased the peak carrier density by almost a factor of 2.

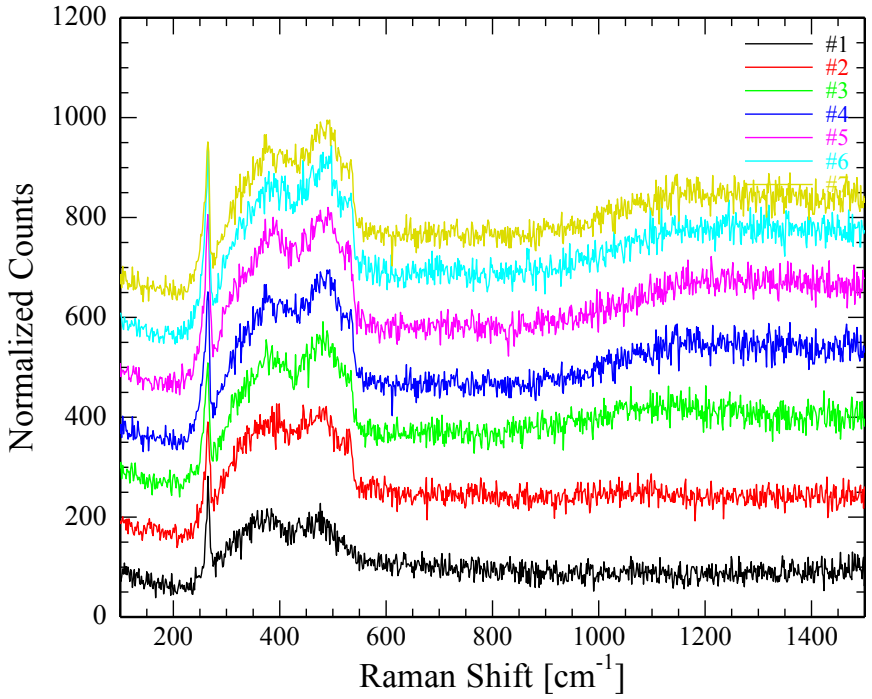

Figure 3.15: LSA on the high dose samples for 5 ms dwell annealing at 75 A current. Scans extend from low temperature (black) at the bottom to the higher annealing temperature (yellow) at the top.

Figure 3.16 shows the LO peak area and LOPCM peak position corresponding to spectra in Figure 3.15. The increase of the LOPCM peak position from 1050 cm^{-1} to 1200 cm^{-1} shows increased activation at the center of the sample, corresponding to the highest temperatures. In contrast, the film quality remains fairly constant as indicated by the relatively constant GaAs LO peak area (Figure 3.16).

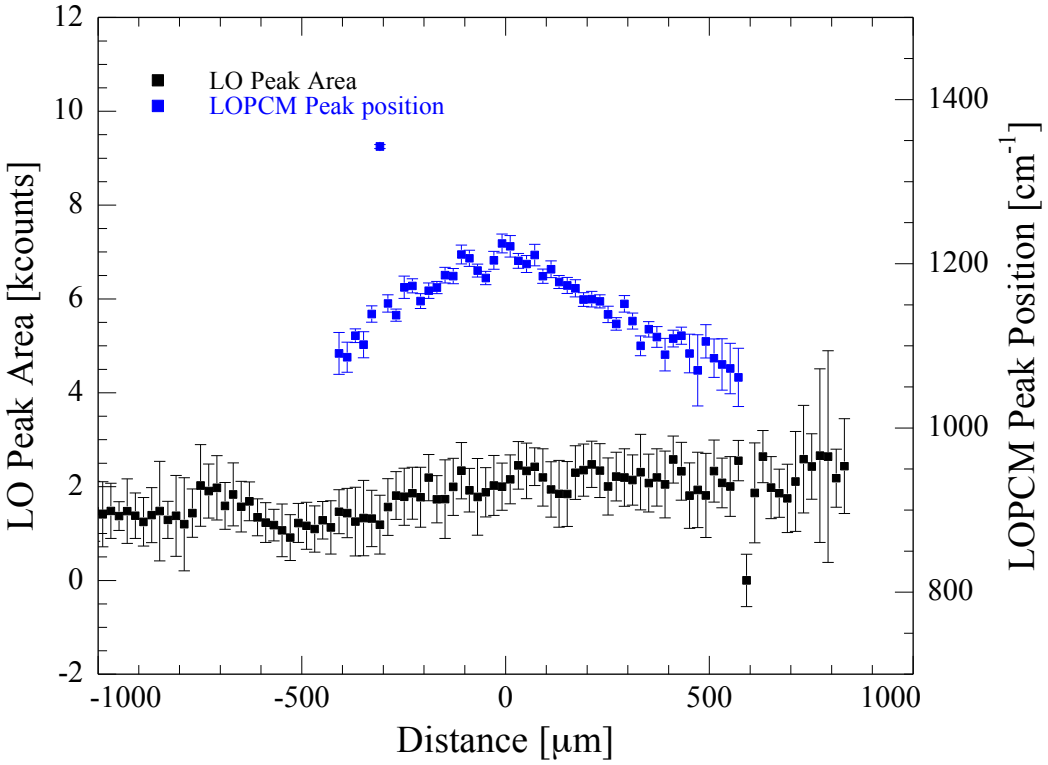

Figure 3.16: LO peak area (black) and LOPCM peak position (blue) for high dose samples annealed for 5 ms at 75 A.

3.7.2 LSA of Ion Implanted High Dose Pre-annealed Samples

As noted above, pre-annealing was performed on several high dose samples: (a) a 750°C spike flash anneal and (b) a 750°C 5 s fast ramp flash anneal. The flash lamp anneal allows rapid heating using a light flash with a duration of a few hundreds of microseconds to milliseconds.

Preannealed sample were significantly different in electrical properties. Sample annealed with the 750°C spike exhibits higher mobility than the samples annealed by the fat ramp. Initial properties of the two samples are shown in Table 3.7.

Table 3.7: Summary of pre-annealed electrical properties prior to LSA

Sample	Before LSA				
	Flash Anneal	**Mobility (cm^2/Vs)**	**Sheet Number (cm^{-2})**	**LOPCM Peak Position (cm^{-1})**	**Estimated Carrier Density (cm^{-3})**
A	750°C Spike	4044	$2.49x10^{12}$	None	$\sim 0.6x10^{18}$
B	750°C 5s fast ramp	1788	$18.6x10^{12}$	~850	$\sim 4.5x10^{18}$

750°C spike pre-anneal after LSA are shown in Figure 3.17. The film quality improves with increasing anneal temperature, and active carrier concentration reaches a maximum at 1300 $cm.^{-1}$ This corresponds to an increase in carrier density by a factor of thirty, from $0.6x10^{18}$ cm^{-3} to $18x10^{18}$ cm^{-3}.

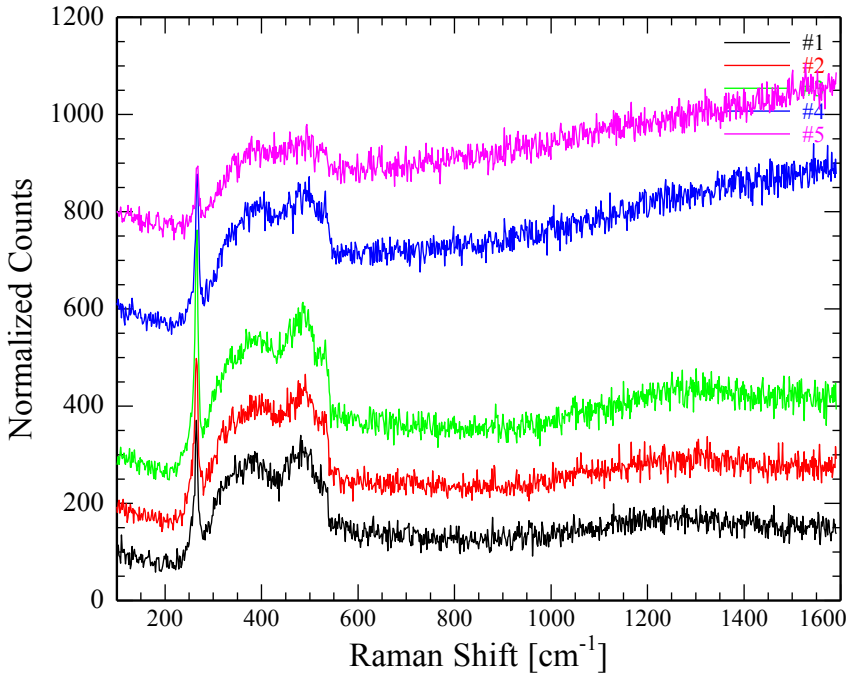

Figure 3.17: Raman spectra of sample A after a 750°C spike pre-annealing and LSA annealing. Annealing temperature increases from the lower (black) to higher (pink) curves. The highest two temperature indicate annealing about the damage threshold as indicated by the loss of GaAs LO phonons.

Figure 3.18 shows the LO peak area and LOPCM peak position as a function of position on the sample. This particular cracked in half as a result of the LSA annealed at 5 ms dwell and 75A. Thus Raman is shown over lonely half of the sample, with the left corresponding to the highest temperature. Dopant activation improves with annealing at higher temperature, as shown in Figure 3.18. The extremely large error bars on the right side of the Figure 3.18 correspond to the onset of damage, where it is estimate the LOPCM peak. Similar trends are observed in LOPCM peak

area and LOPCM peak position data. This is consistent with results observed after laser spike annealing of low dose samples (Figure 3.9).

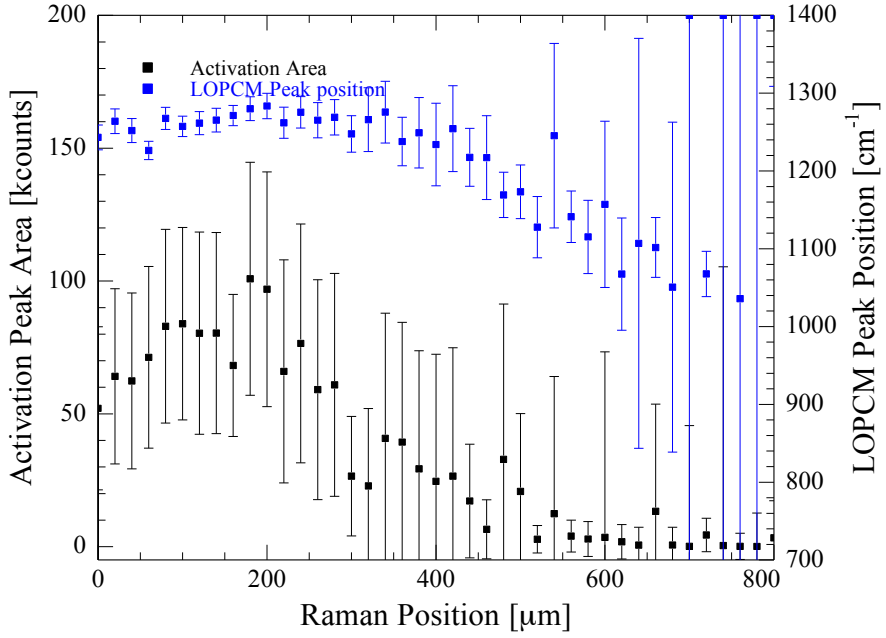

Figure 3.18: LOPCM peak area (black) and LOPCM peak position (blue) as a function of sample position following LSA on pre-annealed samples A.

The second pre-annealed sample, "B", received a 750°C, 5 s, fast ramp flash anneal prior to diode LSA for 5 ms at 75A. Raman spectra are shown Figure 3.19. As for other samples, film quality improved with annealing temperature, and the active carrier concentration increased to near 1200 cm^{-3}. The carrier density thus improved by a factor of ~3, from $4.5x10^{18}$ cm^{-3} to $14x10^{18}$ cm^{-3}.

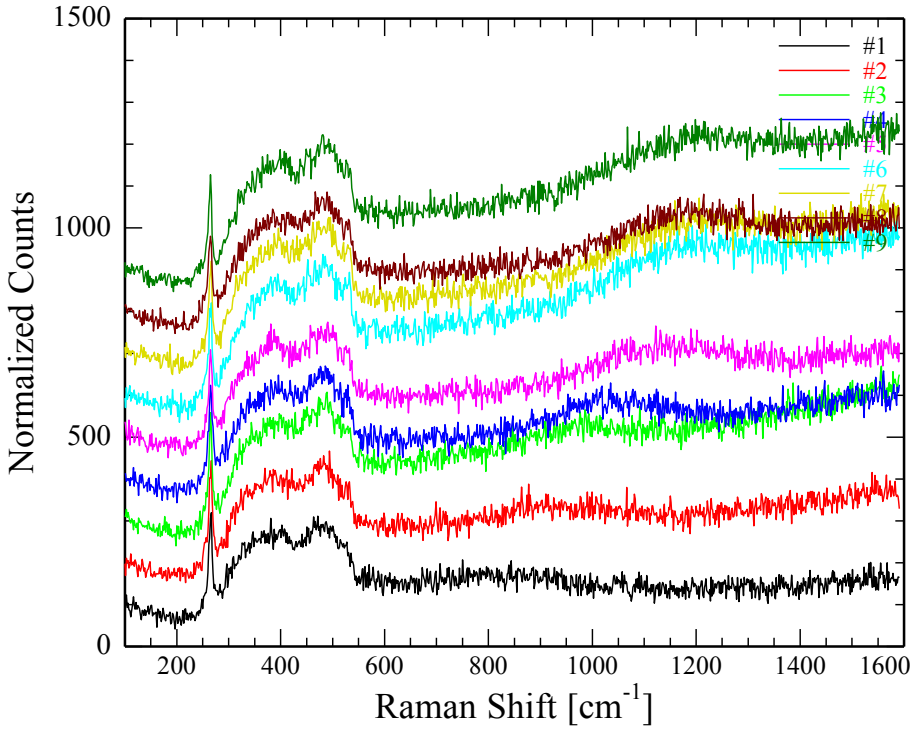

Figure 3.19: Raman specta of after LSA pre-annealed to 750°C, 5 s, fast ramp flash anneal and LSA. Temperature increases from the bottom curve (black) to the top (green). At the highest temperature , damage is observed as indicated by the loss of the GaAs LO peaks.

Figure 3.20 shows the LO peak area and LOPCM peak positions after LSA. As before, the film quality remains fairly constant. The carrier activation increases to nearly a constant level in the center, reaching a maximum of 1200 cm-1 and a carrier density of 1.4 x 10^{19} cm^{-3}.

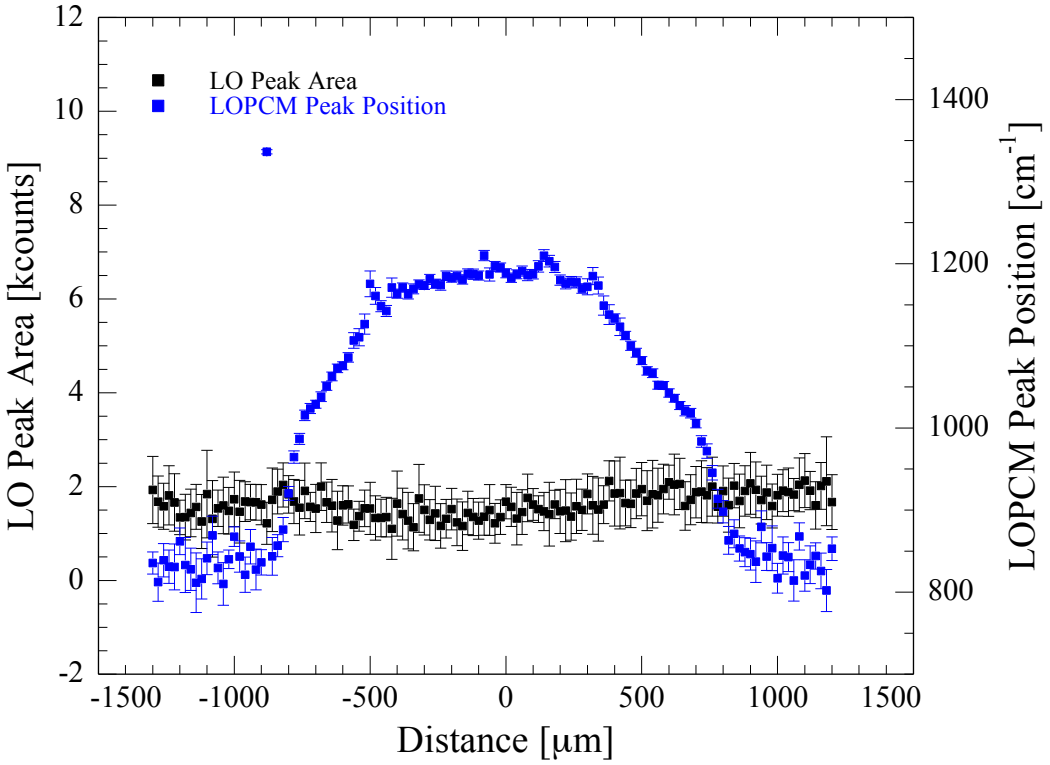

Figure 3.20: LOPCM Peak area (black dots) and LOPCM Peak position (blue dots) for LSA on High Dose Samples B

Comparing the different pre-annealed conditions, we observed that LSA had a greater effect on sample A, though both reached very similar peak activations levels. Post-LSA electrical values are summarized for A and B samples in Table 3.8. Overall, LSA can further improve dopant activation, even after pre-annealing.

Table 3.8: Electrical properties of pre-annealed high dose samples after LSA

Sample	After LSA		
	Pre-Anneal	**LOPCM Peak Position (cm^{-1})**	**Estimated Carrier Density (cm^{-3})**
A	750°C Spike	~1300	~$18x10^{18}$
B	750°C 5s fast ramp	~1200	~$14x10^{18}$

3.7.3 LSA of the MBE High Dose Samples

Figure 3.21 shows Raman spectra of high dose MBE-grown InGaAs samples after diode LSA for 5 ms at 75A. Surprisingly, we observe no deactivation of carrier density. The initial high metastable LOPCM peak position remains essentially unchanged between annealed and unannealed regions. Annealing does result in slightly improved film quality as evidenced by the GaAs LO peak around 270 cm^{-1} and the shoulder peaks in 300-550 cm^{-1} range. The maximum LOPCM of 1550 cm,$^{-1}$ corresponding to an estimated carrier density of $3x10^{19}$ cm^{-3}. This value matches the density determined from a Van der Pauws measurement of $2.86x10^{19}$ cm^{-3} by the University of Florida.

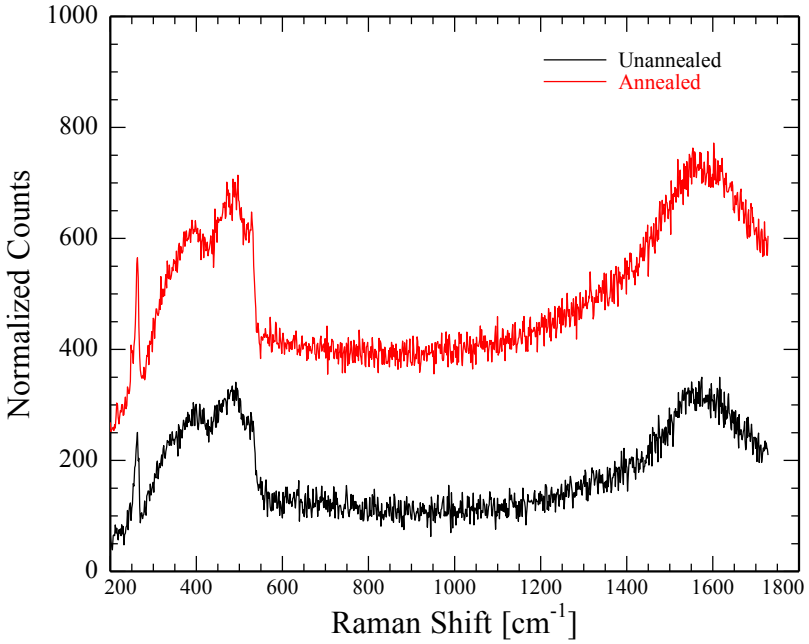

Figure 3.21: Raman spectra of MBE-grown sample showing an unannealed region and a region near the highest annealed temperature.

Figure 3.22 shows the LO peak area and the LOPCM peak position after LSA of the MBE sample. No significant activation or deactivation is observed across the full range of LSA annealing conditions.

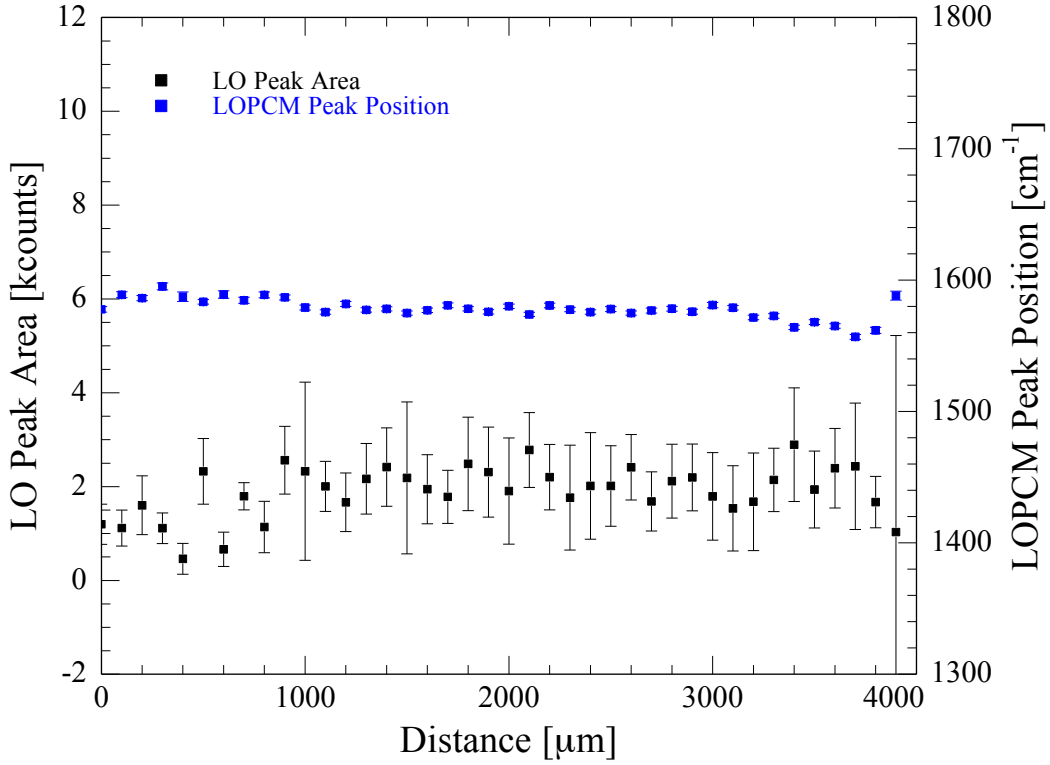

Figure 3.22: LOPCM Peak area (black dots) and LOPCM Peak Positions (blue dots) for LSA on MBE sample from University of Florida

The maximum dopant activation for the high dose samples is summarized in Table 3.9. Activation levels achieved by laser spike annealing exceed those observed for rapid thermal annealing, reaching a maximum carrier density of 1.4×10^{19} cm^{-3}. A two stage annealing process, pre-annealing by RTA followed by an LSA annealed, resulted in higher carrier densities of 1.8×10^{19} cm^{-3}. MBE samples, with initial carrier activations well into the metastable regime, were stable under the short time-scales of laser spike annealing with no observable deactivation at all temperatures. For these MBE samples, carrier densities reached 3.0×10^{19} cm^{-3}.

Table 3.9: Maximum Dopant Activation For High Dose Sample

Sample	**MBE**	**Ion-Implant**	**Ion-Implant+ 750°C spike**	**Ion-Implant+ 750°C, 5s fast ramp**
LOPCM Peak position (cm^{-1})	1550 (no change)	1200	1300	1200
Estimated Carrier Density (cm^{-3})	$3.0x10^{19}$	$1.4x10^{19}$	$1.8x10^{19}$	$1.4x10^{19}$

3.8 Conclusions

Laser spike annealing was studied on a variety samples with different pre-annealing conditions, Si implant doses, and growth method (MBE-grown versus ion-implanted). All samples exhibited enhanced carrier activation following LSA.

LSA is a powerful technique that enables us to probe the annealing behavior, which can be varied as a function of dwell and temperature. We have shown that LSA offers several important advantages compared to furnace annealing and RTA, including an ability to reach higher annealing temperatures prior to damage and enhanced Si dopant activation.

Comparing the low and high Si dose samples, we found that the extent of dopant activation is implant concentration-dependent. Importantly, we also showed that LSA did not degrade metastable Si dopant concentration achieved by MBE; this is in contrast to other annealing methods, which show a steady decrease in dopant

concentration (deactivation) as a function of temperature. This finding is potentially important for commercialization of InGaAs devices, which will experience later annealing steps.

We have also found that Raman spectroscopy is a very effective, easy to operate, non-invasive method to probe the film quality and dopant activation. Dopant activation levels can be readily determined from Raman shifts of LOPCM peak.

REFERENCES

[1] Ma, Xuetian. *Sub-millisecond Laser Spike Annealing of $In_{0.53}Ga_{0.47}As$*. Diss. 2014.

[2] Dinges, H. W., H. Burkhard, R. Lösch, H. Nickel, W. Schlapp. "Refractive indices of InAlAs and InGaAs/InP from 250 to 1900 nm determined by spectroscopic ellipsometry." *Applied surface science* 54 (1992): 477-481.

[3] De Wolf, Ingrid. "Micro-Raman spectroscopy to study local mechanical stress in silicon integrated circuits." *Semiconductor Science and Technology* 11.2 (1996): 139.

[4] Hernández, S., B. Marcos, R. CuscoH, N. Blanco, G. GonzaHlez-DmHaz, L. ArtuHs,. "Lattice damage study of implanted InGaAs by means of Raman spectroscopy." *Journal of luminescence* 87 (2000): 721-723

[5] Artus, L., R. Cuscó, J. Ibáñez, J. M. Martin and G. González-Díaz. "Raman-scattering criteria for characterization of anneal-restored zinc blende single crystals: Application to Si^+-implanted InP." *Journal of applied physics* 82.8 (1997): 3736-3739.

[6] Sorg, Victoria, Suki Naifang Zhang, Megan Hill, Paulette Clancy and Michael O. Thompson. "(Invited) Dopant Activation and Deactivation in InGaAs during Sub-Millisecond Thermal Annealing." *ECS Transactions* 66.4 (2015): 117-124.

[7] Thompson, M. O. "GENPLOT and RUMP documentation, 1996." *URL: http://www. genplot. com/doc/index. htm.[46] JF Ziegler, computer code TRIM, URL http://www. research. ibm. com/ionbeams*.

CHAPTER 4

ELECTRICAL MEASUREMENT

4.1 CAPRES Measurement

Direct electrical measurements of LSA annealed samples were made using the CAPRES system. CAPRES measures the sheet resistance and conductance of Si^+ implanted InGaAs samples at a resolution of 20 μm using micro four point probes. The electrical measurements were used to confirm the carrier activation level estimated using Raman spectroscopy in the last chapter. Low dose IBM samples, after LSA using CO_2 laser at 1ms dwell, were exanimated by CAPRES.

Sheet conductance (G_s) and sheet resistance (R_s) are inversely related to each other and measure the total resistivity via

$$R_s = \frac{1}{G_s} = \frac{\rho}{t} \qquad (4.1)$$

where ρ is the risityivity and t is the film thickness. Figure 4.1 show an SEM image of a mircro four point probe. This CAPRES four point probe was scan across the annealing region to determine the resistivity as a function of position.

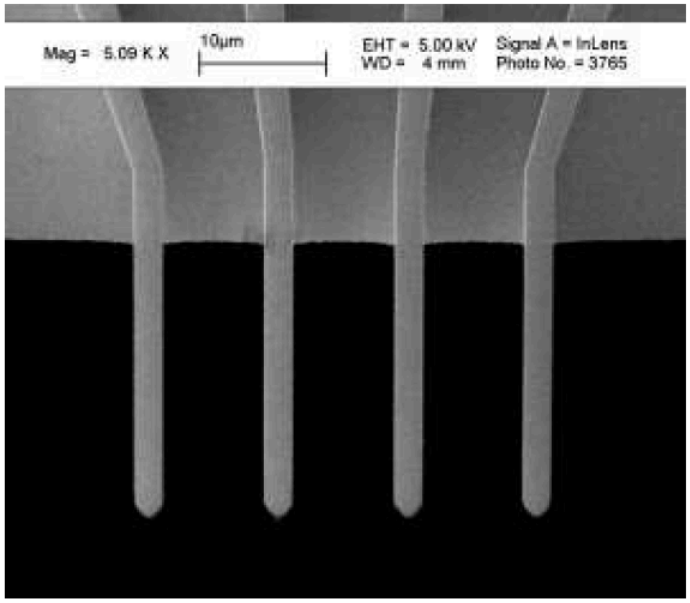

Figure 4.1: SEM image of CAPRES micro four point probe. The probes contact the InGaAs sample allowing 4-pt measurements of the InGaAs sheet resistance [Reproduced from reference 1].

Figure 4.2 shows a schematic set-up of the 4-point probe measurement. Current (I) passes through the outer probes and induces a voltage (V) changes the inner probes. R_s can be calculated as

$$R_s = \frac{\rho}{t} = k(\frac{V}{I}) \qquad (4.2)$$

where k is the geometric factor, V is the voltage and I is the current. For uniformly spaced probe, on a semi-infinite sheet, k=4.532.

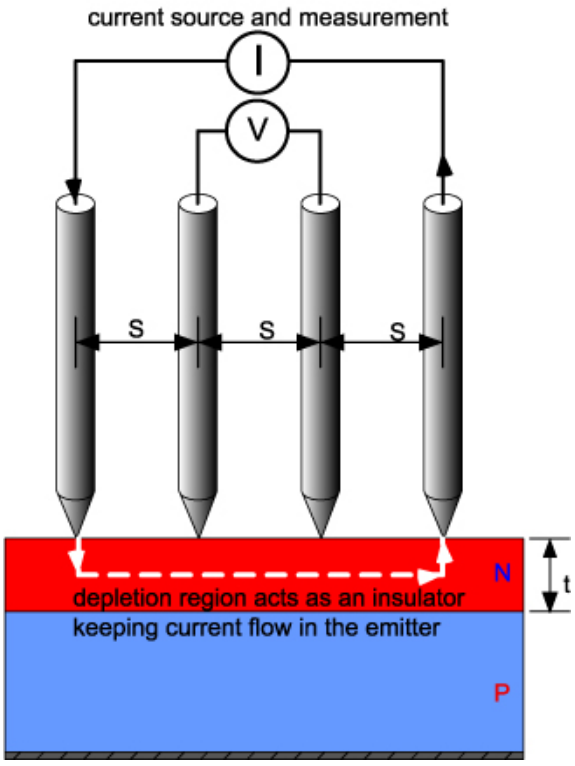

Figure 4.2: schematic set-up to measure sheet resistance [Reproduced from reference 2].

4.2 Comparison With Raman Results

CAPRES micro four point probe measurements were taken as a function of position across laser spike annealing region to confirm the dopant activation level on the Si^+ implanted InGaAs after laser spike annealing.

Figure 4.3 shows the CAPRES results on samples CO_2 LSA annealed at 1ms 22W and 1ms 24W. Data are plotted as sheet conductance, which is proportional to the carrier density, with sheet resistance shown on the right axis. The anneal at 22 W below the damage threshold yielding the maximum activation at the laser center. In contrast, 24 W is above the damage threshold and the sheet conductance drops in the

center region with maximum activation located on the wings near $\pm 65\ \mu$m. A minimum sheet resitance of 135 Ω/ □was observed with high activation occurring near the damage threshold.

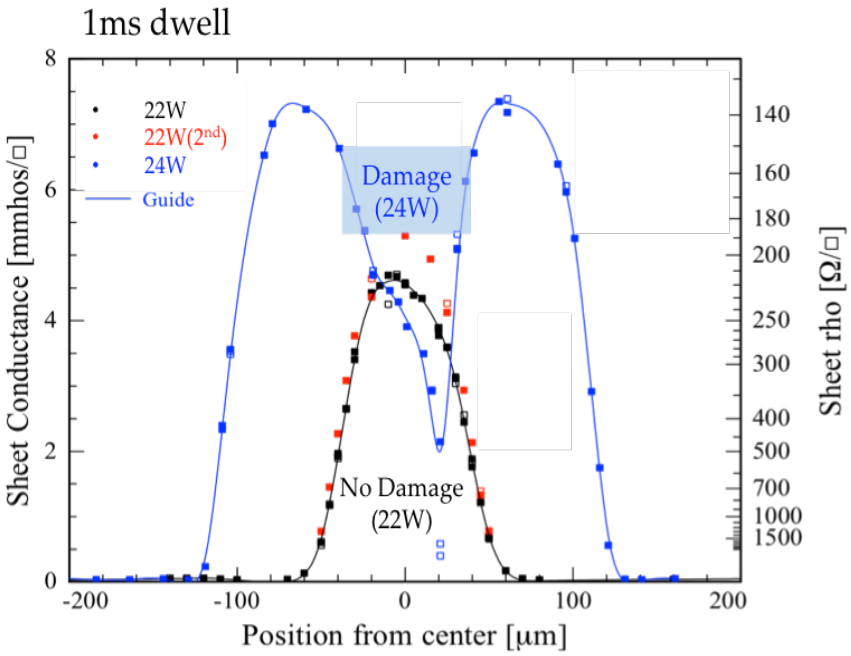

Figure 4.3: CAPRES measurement on 1ms 22W (red) and 1ms 24w (blue) CO_2 LSA Samples. A minimal resistance of 135 Ω/□ was observed.

Figure 4.4 plots the sheet conductivity and sheet resistivity in terms of annealing temperature after LSA. The onset of activation is near 795 ^{o}C with peak activation near 850 ^{o}C and damage above 865 ^{o}C. Although the 1ms 22W annealed samples does not reach the highest conductance, the data follow that for 1ms 24W annealed. This further confirms the reliabilities of temperature measurement under LSA.

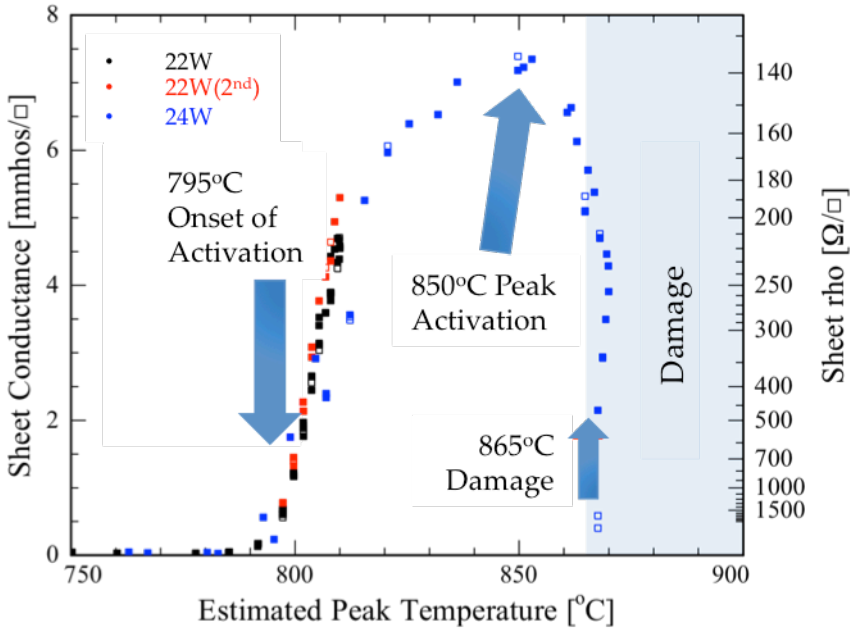

Figure 4.4: CAPRES results as a function of temperature. Peak activation occurs near 850 °C. The 1ms 22 W (red and black) and 1ms 24 (blue) data overlay confirms the temperature calibrations.

Figure 4.5 compares the two estimates of dopant activation as a function of temperature and the electrical conductance matches well with the estimated carrier density from the LOPCM peak position. The same trend is observed between these two analyses.

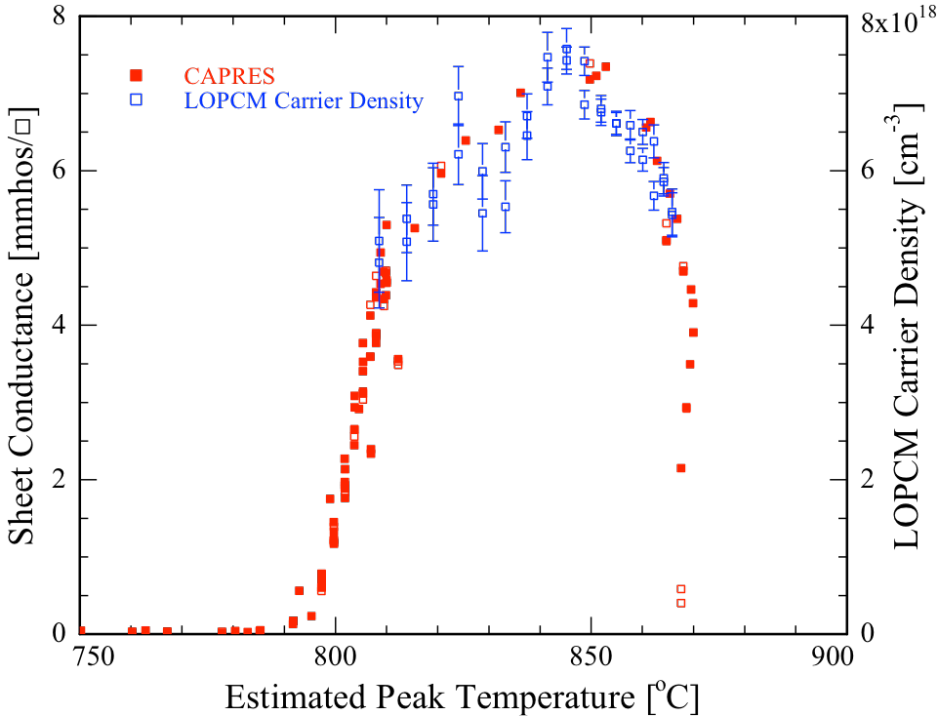

Figure 4.5: Raman estimate of carrier density Vs. CAPRES electrical measurement of sheet resistance. The CAPRES data (red) and the carrier density estimated by the LOPCM peak position by Raman analysis (blue) matches well between these two analyses.

REFERENCES

[1] Petersen, Christian L., Burnaby, BC ; Lin, Rong ; Petersen, D.H. ; Nielsen, P.F. "Micro-scale sheet resistance measurements on ultra shallow junctions." *Advanced Thermal Processing of Semiconductors, 2006. RTP'06. 14th IEEE International Conference on*. IEEE, 2006.

[2] http://pveducation.org/pvcdrom/characterisation/four-point-probe-resistivity-measurements

CHAPTER 5

CONCLUSIONS

InGaAs is considered a potential interim solution for device scaling to enable continued progress along Moore's Law. However, dopant activation remains a critical challenge. This work explored the use of sub-ms Laser Spike Annealing as an alternative to other thermal annealing processes. The short annealing time scale was likely to permit metastable activation of dopants beyond the limits of furnace anneals and RTA anneals.

In this project, the behavior of both low-dose and high dose Si ion-implanted $In_{0.53}Ga_{0.47}As$ under laser spike annealing was studied. Temperature during LSA was determined using spatially resolved thin-film resistors, allowing temperature profiles across an each individual laser annealed stripes to be established. This enable combinational like characterization of the annealing behavior. Low dose samples were annealed using the CO_2 LSA system or in a furnace, while high dose samples were annealed using a diode based LSA system.

Overall, LSA was found to extend temperature limits for annealing InGaAs and to enhance dopant activation for both low dose and high dose samples. Low dose samples implanted to a peak concentration of 2.7×10^{19} cm^{-3} showed maximum activation at 8×10^{18} cm^{-3} corresponding to 29.6 % activation. High dose samples implanted to a peak concentration of 1×10^{20} cm^{-3} showed maximum activation at 1.8×10^{19} cm^{-3} corresponding to 18 % activation. These results demonstrate that LSA has

the potential to solve one of the critical challenges facing use of InGaAs in future device technologies.

APPENDIX

A.1 Experimental Procedures During LSA

Figure A.1 shows a schematic of InGaAs samples during LSA. InGaAs samples were cut in 6 x 6 mm square mounted between two pieces of Si. These Si pieces were necessary to prevent the laser beam from hitting and damaging the stage. Cu tape was used to hold the InGaAs samples and prevent cracking due to the excess heat at the sample edge. Configured in this way, the laser beam scan starts on the Si piece, then scans the InGaAs sample, and finally moves to the bottom Si piece.

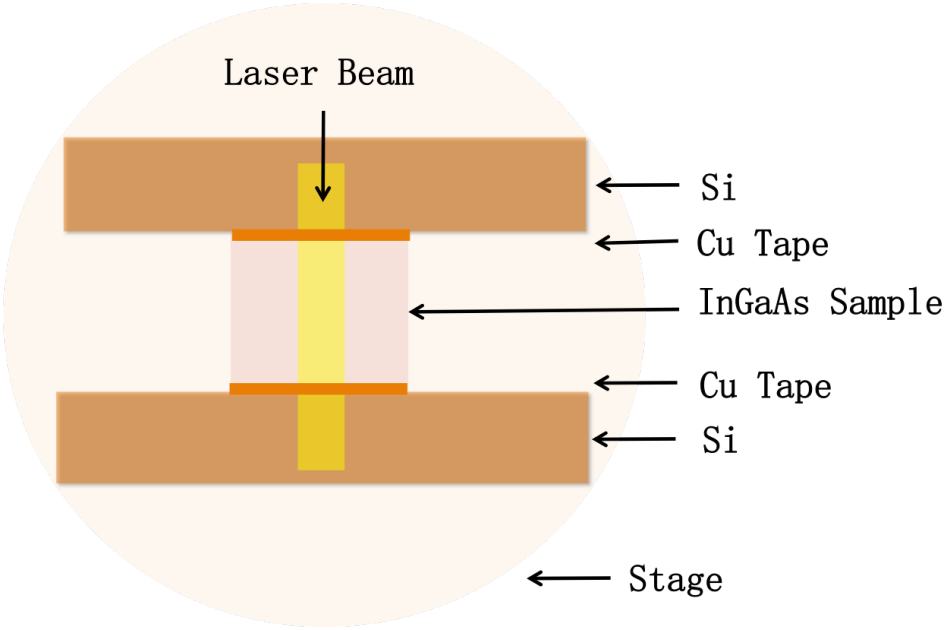

Figure A.1: Schematic layout of an InGaAs samples during LSA.

Typical annealing conditions for CO_2 LSA and Diode LSA are listed in Table A.1 [1].

Table A.1: Typical annealing conditions for CO_2 LSA and Diode LSA

	Dwell	**Power / Current**
CO2	250 us	36-44 W
	500 us	20-30 W
	1 ms	18-26 W
	2 ms	14-22 W
Diode	5 ms	66-75A

A.2 Experimental Procedures During Raman Spectroscopy

Typical procedures to collect Raman spectra on InGaAs samples are given below.

1. Raman manual provided by CCMR was followed to check Raman spectroscopy conditions before actual measurement.
2. The specific laser source for Raman measurement was chosen 488 nm or 532 nm. With the new Rayleigh filters, the 488 nm laser is preferred as it is easier to use compared to the 532 nm laser. The 532 nm source requires additional training and the filter must be changed manually each time. .
3. Prior to InGaAs measurements, a Si reference scan was taken to compare Raman spectra collected at different times. Si samples can be found in the Raman room. The Si reference scan was taken under 1s acquisition time with 1 accumulations. Typical signals at the Si characteristic peak (520 cm^{-1}) are around ~5000 counts.
4. The InGaAs sample was taped to a glass slide (double side) to hold the samples stationary during measurements. A single point scan or a mapping scan using 3s

acquisition time and 4 accumulations was generally used to minimize noise and obtain good signal. For high quality spectra, a 3s acquisition time and 40 accumulations was used; these spectra showed almost all of the peaks in InGaAs spectra.

5. Following InGaAs measurements, an additional Si reference scan was often collected. Comparing the 1st and 2nd Si reference scans ensured the stabilization of the Raman system during the actual InGaAs measurements.

A.3 Capping Layer Effect

A study of the effect of an Al_2O_3 capping layer (to prevent arsenic loss) during LSA is shown in Figure A.1. Both CO_2 and diode based LSA was used to anneal samples with and without capping layer. For CO_2 annealing, only IBM provided low dose samples were used. The capping layer was deposited by collaborators at the University of Florida using the conditions as for high dose samples.

Figure A.2 shows optical images of samples annealed under identical conditions. The capping layer has some effect, but does not s prevent the arsenic loss as there are similar visual damages observed after CO_2 and diode irradiation.

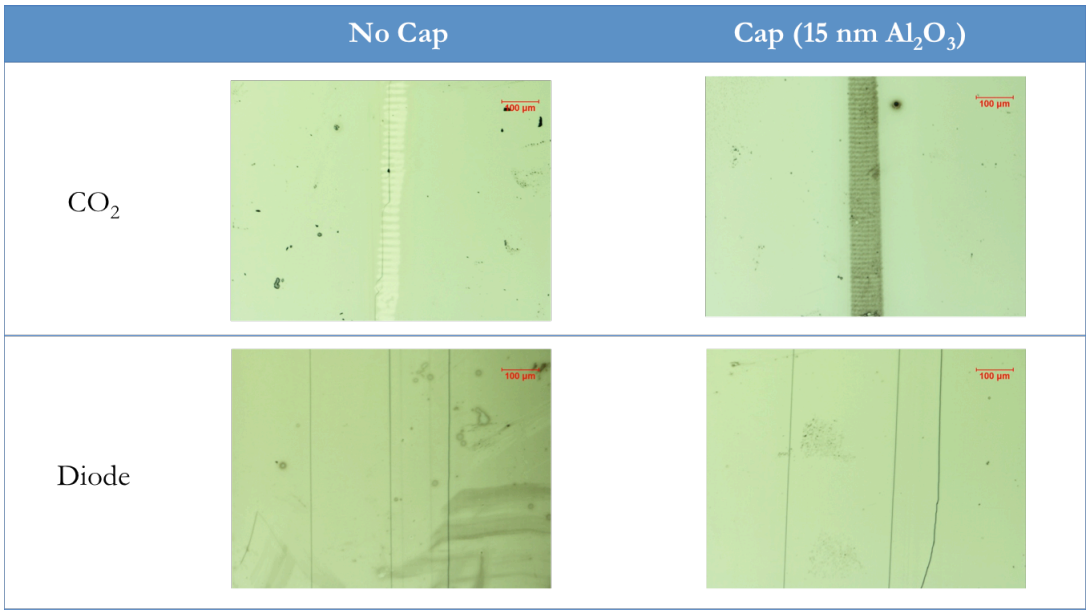

Figure A.2: Capping layer effect for samples with and without capping layers, annealed by both CO_2 and diode laser. No obvious change was observed.

Figure A.3 shows Raman analysis of the LOPCM peak area and position for a sample annealed by CO_2 without a capping layer. Figure A.4 shows similar data for a sample with a capping layer. Comparing Figures A.3 and A.4, the capping layer does not prevent damage at the center of the annealing region. However the shape of the graph is slightly different. In Figure A.3, without the capping layer, the LOPCM peak position decreases before damage. However in Figure A.4, with the capping layer, the LOPCM peak position remains high right up to the damage region.

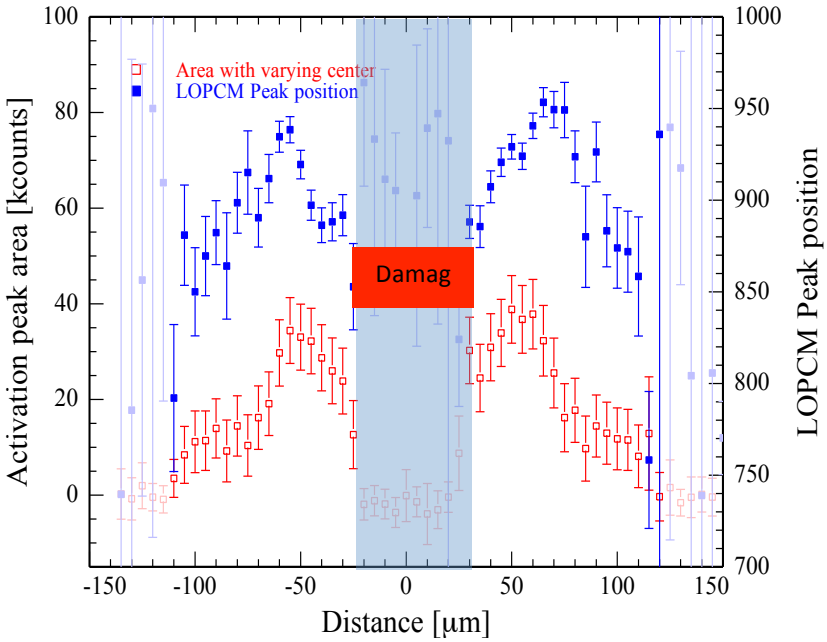

Figure A.3: Raman analysis on the LOPCM peak area and LOPCM peak position for sample annealed by CO_2 laser without a capping layer

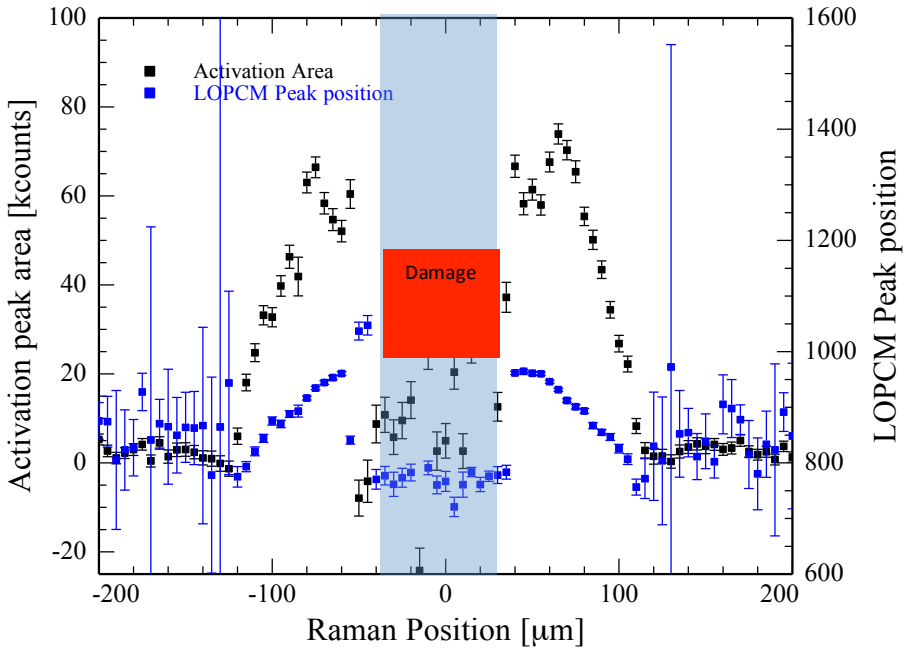

Figure A.4: Raman analysis on the LOPCM peak area and the LOPCM peak position for a sample annealed by CO_2 laser with a capping layer

A.4 Diode Polymer Calibrations

Pt thermistors measurement for the diode based LSA were difficult. As there were existing measurements on Si, a polymer decomposition measurement was used to estimate annealing temperature for InGaAs samples.

The thermal decomposition of a photoresist S1815 was used. Since the decomposition temperature showed is nearly identical for all substrates, the diode laser, with a wavelength of 980nm, is sensitive to the thickness of photoresist. To minimize thin film interference effect, the bare samples should have the same reflectivity as a photoresist coated sample. Figure A.5 shows the reflectivity of various samples as a function of wavelength. At 980 nm, both InGaAs and Si samples, with or without photoresist, have a 33% reflectivity.

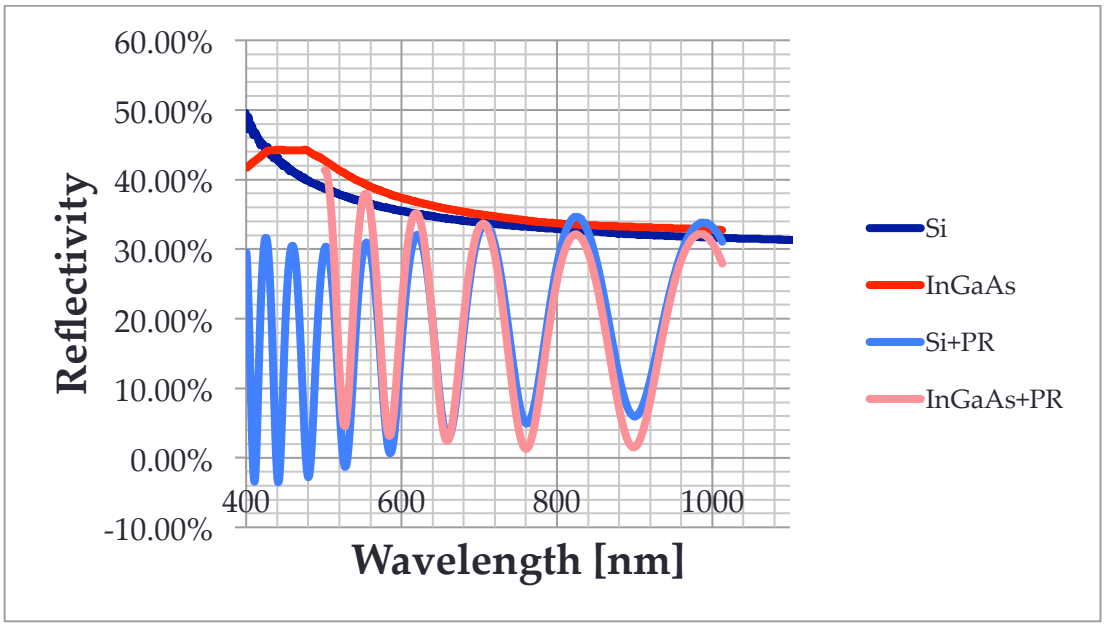

Figure A.5: Reflectivity study for silicon wafer and InGaAs sample under diode annealing

The optimal photoresist, thickness was 1500 nm. Figure A.6 shows LSA stripes at various powers. Comparing the width of the decomposed resistor, we found that 5 ms 30A on InGaAs achieved the same conditions as 5 ms 37A on silicon.

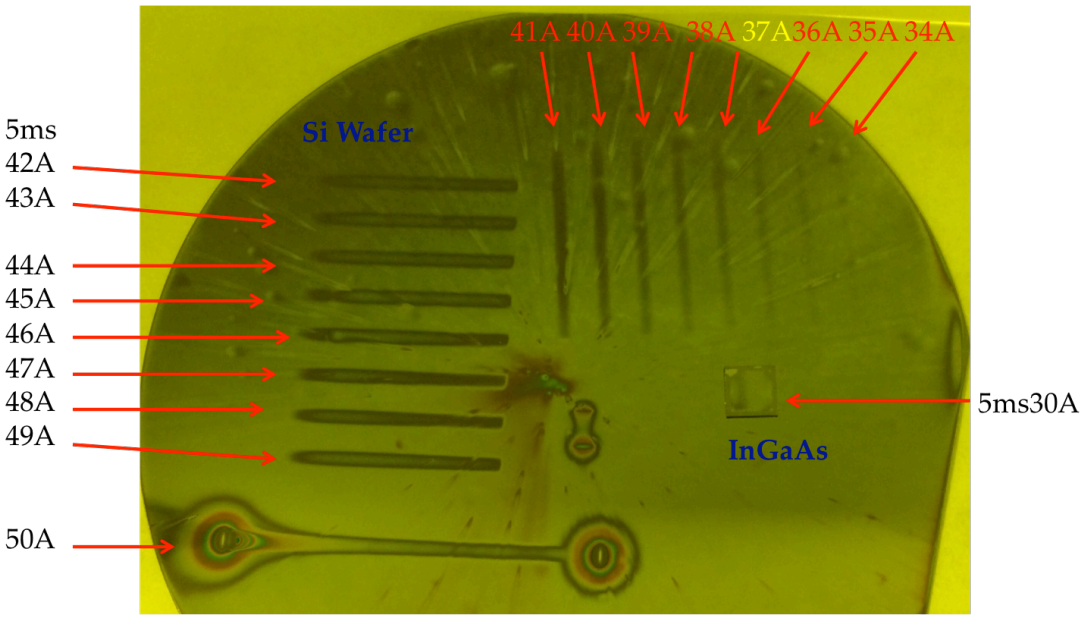

Figure A.6: Polymer calibration for diode annealing. The behavior of photoresist on InGaAs is compared with a Si wafer during diode annealing

A.5 MBE vs. Ion Implantation

Figure A.7 shows the schematic of dopant incorporation into the substrate during the ion implantation process. Si dopants are bombarded into the surface of the InGaAs samples generating numerous defects; in addition the Si dopant can sit on interstitial and substitutional sites. Post annealing process is needed to restore the film quality and allow the Si dopants to find cation sites.

Figure A.8 schematically shows dopant incorporation during MBE process. Si dopants are grown into the lattice with In, Ga and As species at a elevated temperature in a layer by layer. The crystalline structure remains intact and Si is incorporated into cation sites resulting in a metastable state.

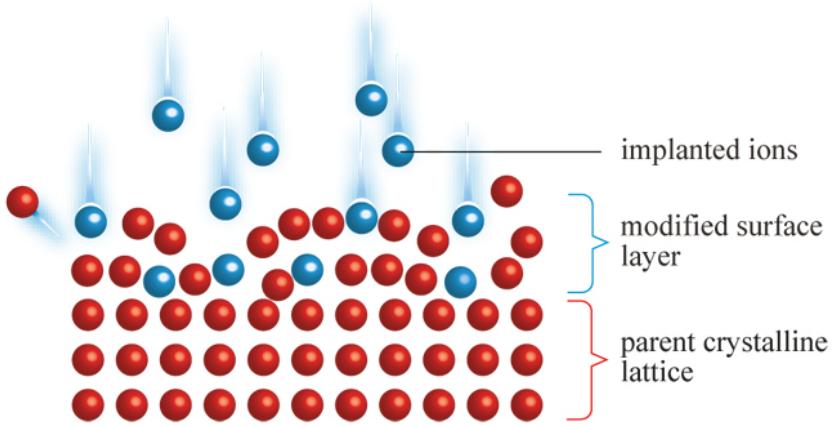

Figure A.7: The ion implantation process [2]

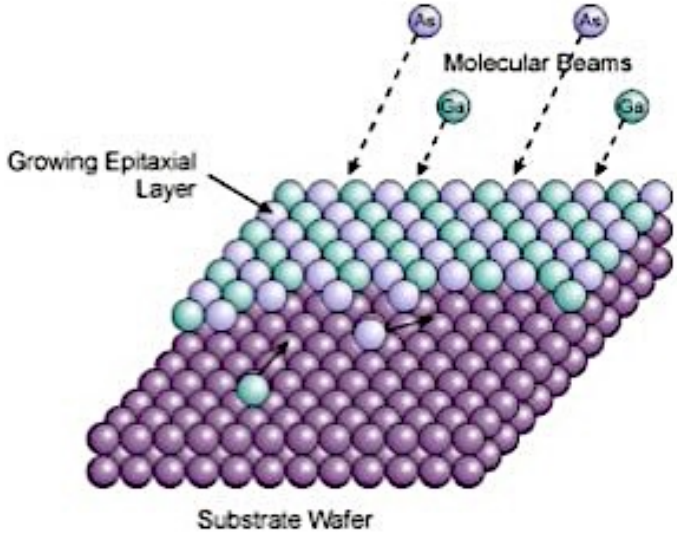

Figure A8: The dopant incorporation during the MBE process [3]

REFERENCES

[1] Ma, Xuetian. *Sub-millisecond Laser Spike Annealing of In0. 53Ga0. 47As*. Diss. 2014.

[2] http://eng.thesaurus.rusnano.com/wiki/article887

[3] https://www.ee.ucl.ac.uk/about/MBE